工學博士學位論文

Fabrication of Fluorescent Hybrid Nanoparticles and Their Specific Ion and Molecule Detection Applications

형광 하이브리드 나노 입자 제조 및 특정 이온 및 분자 검출 응용

2016年 8月

서울大學校 大學院

化學生物工學部

李 仁 圭

↑
2cm
↓

Fabrication of Fluorescent Hybrid Nanoparticles and Their Specific Ion and Molecule Detection Applications

2016年

李仁圭

↑
2.5cm
↓

↑
4cm
↓

↑
3cm
↓

↑
2cm
↓

Fabrication of Fluorescent Hybrid Nanoparticles and Their Specific Ion and Molecule Detection Applications

by

Inkyu Lee

Submitted to the Graduate School of Seoul National University

in Partial Fulfillment of the Requirements

for the Degree of Doctor of Philosophy

August, 2016

Thesis Adviser: Jyongsik Jang

ABSTRACT

Various nanoprobe systems are being developed to explore their potential in biomedical fields, with many applications to the diagnosis or monitoring of various diseases. There are many advantages of nano-size probes for the application in biomedical field. First, the scale of cell and tissue structures is meaningful. Since most nanoprobes are about 10—500nm which are generally over 100 fold smaller than cells. Second, the building blocks of nanoprobes like proteins, carbohydrates, nucleic acids, synthetic polymers or small inorganic particles are generally smaller than about several scores of nanometers. Third, nanoprobes have potential for wide application because they can easily contain useful molecules such as imaging agents, active targeting moieties, or drugs by simple loading or conjugation. Consequently, it is still challenging to produce fluorescent hybrid nanoparticles for detecting and imaging target analytes in living systems.

This dissertation describes the three different ways in the synthetic methodology of fluorescent hybrid nanoparticles. First, PAN nanomaterials as novel bioimaging agents without additional fluorophores were developed by ultrasound induced emulsion polymerization, and it could be applied for the

fluorescence sensors of copper ion and cell imaging. Second, a dual emission Au-PAN NPs sensor was prepared for sensitive detection of mercury ions in aqueous solution. The Au-PAN nanoparticles showed significant intensity change by addtion of mercury ions and higher binding affinity toward mercury ion than other metal ions. Lastly, a novel fluorescent Au-GQDs nanoparticle was synthesized for use as a probe that can selectively detect Cys in living cells. The dual emission fluorescence peak ratio changed when the Au-GQDs nanoparticles reacted with Cys. This fluorescence behavior was highly specific for Cys. Most importantly, these novel approaches can be used as an alternative tool for specific ions and molecule detection in environmental condition, and may offer an opportunity for the further investigation of industrial applications, and might be expanded to allow the fluorescence sensor applications of hybrid nanoparticles in a wide range of areas.

KEYWORDS: Fluorescent hybrid nanoparticle; Surface modification; Gold nanocluster; Graphene quantum dots; Cell imaging; Fluorescence detection

STUDENT NUMBER: 2013–31307

List of Abbreviations

A : absorbance at the excitation wavelength

$Al(NO_3)_3$: aluminium nitrate

AN : acrylonitrile

$AgNO_3$: silver nitrate

ATP : adenosine triphosphate

AuNCs : gold nanocluster

$CaCl_2$: calcium chloride

$CdCl_2$: cadmium chloride

CNF : carbon nanofibers

$CoCl_2$: cobalt(II) chloride

$CuCl_2$: copper(II) chloride

Cys : cysteine

d : particle diameter

EDC : 1-ethyl-3-(3-dimethylaminopropyl)-carbodiimide

F : integrated area of emitted fluorescence spectra

$FeCl_2$: iron(II) chloride

$FeCl_3$: iron(III) chloride

FTIR : fourier transform infrared

FR : folate receptor

GQDs : graphene quantum dots

GSH : L-glutathione

$HAuCl_4$: gold(III) chloride trihydrate

HCl : hydrogen chloride

HCys : homocysteine

$HgCl_2$: mercury(II) chloride

H_2SO_4 : sulfuric acid

H_2O_2 : hydrogen peroxide

HCl : hydrochloric acid

KBr : potassium bromide

KCl : potassium chloride

LOD : limit of detection

$MgCl_2$: magnesium chloride

$MnCl_2$: manganese(II) chloride

MPA : mercaptopropionic acid

$NaBH_4$: sodium borohydride

NaCl : sodium chloride

Na_2CO_3 : sodium carbonate

Na_2SO_4 : sodium sulfate

NHS : N-hydroxysuccinimide

$NiCl_2$: nickel(II) chloride

PAN : polyacrylonitrile

$Pb(NO_3)_2$: lead(II) nitrate

PBS : phosphate buffered solution

PEG : polyethylene glycol

PL : photoluminescence

ROS : reactive oxygen species

SEM : scanning electron microscope

SDS : sodium dodecyl sulfate

TEM : transmission electron microscopy

tPAN : surface-treated PAN nanoparticles

UV-vis : ultraviolet-visible spectrophotometry

vol% : volume fraction

wt% : weight content

XPS : X-ray photoelectron spectroscopy

$ZnCl_2$: zinc chloride

λ : wavelength

λ_{em} : wavelengths of emission

λ_{ex}: wavelengths of excitation

σ : standard deviation

Φ : fluorescence quantum yield

List of Figures

wavelength.

Figure 15. The side reaction in the surface modification for the amidine group. When cyano-groups of PAN react with water, it changes to ester group. Then amidine group reacts with ester group on the tPAN NPs surface, turning into Schiff base which contributes to enhanced fluorescence. Therefore, diverse functional groups including amidine and Schiff bases.

Figure 16. The interference effect of different metal ions (10 μM) on tPAN NPs for Cu^{2+} detection.

Figure 17. FT-IR spectra of tPAN NPs+Fe^{2+} (black), tPAN NPs+Fe^{3+} (red), tPAN NPs+Hg^{2+} (blue) and tPAN NPs + Zn^{2+} (violet).

Figure 18. UV–vis absorption spectra of tPAN NPs (10 μg mL^{-1}) upon addition of various metal ions (10 μM) in aqueous solution. Addition of Cu^{2+} resulted in a significant change indicating that the tPAN NPs have higher binding affinity toward Cu^{2+} than other metal ions.

Figure 19. (a) Selectivity of tPAN NPs (10 μg mL^{-1}) for different metal ions (10 μM). Inset represents the possible sensing mechanism of tPAN NP for Cu^{2+}. (b) Fluorescence emission spectra of tPAN NPs in the presence of Cu^{2+} at different concentrations (0-100 μM). (c) Based on the Figure 5b, the relationship between emission fluorescence

intensity of tPAN NPs and concentrations of Cu^{2+} was calculated. *I* and I_0 are the emission fluorescence intensities of the tPAN NPs at 410 nm (λ_{ex}=290 nm) in the presence and absence of Cu^{2+}, respectively. Inset is the linear region. (d) Representative fluorescence spectra with the addition of Cu^{2+} and EDTA in the quenching recovering. The inset shows the fluorescence photograph of tPAN NPs, tPAN NPs + Cu^{2+}, and tPAN NPs + Cu^{2+} + EDTA under UV light (365 nm).

Figure 20. Live cell differential interference images of tPAN NPs-treated SK-BR-3 cells; (a) images are before treatment of Cu^{2+}, (b) images are 20 min after treatment of 10 μg/mL Cu^{2+} and (c) images are 20 min after treatment of 100 μg/mL EDTA. Scale bars = 50 μm.

Figure 21. Fluorescence emission spectra of tPAN NPs with the addition of Cu^{2+} (10 μg mL^{-1}).

Figure 22. Viability of SK-BR-3 cells incubated with tPAN nanoparticles for 24 h. The viability was calculated relative to a negative control. ROS production by SK-BR-3 cells after being incubated with tPAN. H_2O_2 (0.02%) was used as a positive control. Values exhibit mean ± SD, and each experiment was performed in triplicate.

Figure 23. Schematic diagram of fabrication of tPAN NPs and Au-PAN NPs.

Figure 24. TEM images (a) AuNCs, (b) PAN NPs and (c) Au-PAN NPs. AuNCs and tPAN NPs were uniform sphere in shape After decoration of AuNCs on the surface of the tPAN NPs, the dark spots.

Figure 25. (a) FTIR spectra of PAN (black), tPAN (red), and Au-PAN NPs (blue). (b) XPS spectra of PAN (black), tPAN (red), and Au-PAN NPs (blue). (c) Enlarged Au 4f spectrum of Au-PAN NPs.

Figure 26. (a)UV-vis absorprion spectra and (b) the representative fluorescence spectra of the AuNCs (black), tPAN (red), and Au-PAN NPs (blue).

Figure 27. The emission ratio (I_{420}/I_{570}) of Au-PAN NPs (50 μg mL^{-1}) in the presence of various analytes (10 μM) in PBS for 60 min. A) blank; B) Hg^{2+}; C) Cu^{2+}; D) Al^{3+}; E) Ni^{2+}; F) Cr^{2+}; G) Co^{2+}; H) Pb^{2+}; I) Fe^{2+}; J) Mg^{2+}; K) Zn^{2+}; L) Cd^{2+}; M) Sr^{2+}; N) Ca^{2+}; O) Fe^{3+}; P) K^{+}; Q) Li^{2+}.

Figure 28. The interference effect of different metal ions (10 μM) on tPAN NPs for Hg^{2+} detection.

Figure 29. (a) Fluorescence emission spectra of Au-PAN NPs in the presence of Hg^{2+} at different concentrations (0-200 nM). (b) Based on the Figure 32a, the relationship between emission fluorescence intensity

in the presence of Cys at different concentrations. (b) Based on the Figure 39a, the relationship between emission fluorescence intensity of FA-Au-GQDs and concentrations of Cys/Hcy was calculated. Inset is the linear region.

Figure 38. Time-dependent fluorescence intensity plot of FA-Au-GQDs after Cys/Hcy insertion (5 nM; detected at 435 nm emission and 580 nm, respectively).

Figure 39. Fluorescence images of SK-BR-3 cells treated with FA-Au-GQDs (0.05 mM).; (a) from blue channel of cells; (b) from red channel; (c) Bright field images (d) fluorescence image. Fluorescence images of MCF-7 cells treated with FA-Au-GQDs (0.05 mM).; (e) from blue channel of cells; (f) from red channel; (g) Bright field images (h) fluorescence image. (i) from blue channel of cells incubated with Cys (0.04 mM) for 30 min; (j) from red channel; (k) Bright field images (l) fluorescence image.

Figure 40. (Red) ROS production by MCF-7 cells after being incubated with FA-Au-GQDs. H_2O_2 (0.02%) was used as a positive control. (Blue) Viability of MCF-7 cells incubated with FA-Au-GQDs for 24 h. The viability was calculated relative to a negative control. Values exhibit mean ± SD, and each experiment was performed in triplicate.

Table of Contents

1. INTRODUCTION

1.1. Background

1.1.1. Nanoprobe

Recently, various nanoprobe systems are being developed to explore their potential in biomedical fields, with wide applications to the diagnosis or diseases monitoring. [1] There are many advantages of nano-size probes for the application in biomedical field. First, the scale of cell and tissue structures is meaningful. Since most nanoprobes are about 10—500nm which are generally over 100 fold smaller than cells, their sizes are of the same or lower order of magnitude compared with that of the pores and openings in vasculature and tissues of human body. [2] Nonoprobes uptake by kidney (renal clearance) was lower than single molecules and the uptake by reticularendothelial system (RES) of liver was lower than micro-size materials [3]. Therefore, nano materials show circulation time increase and have more chances to reach the target site than single molecules. In addition, nanoprobes efficiently accumulate at the vascular angiogenic sites like tumor and arthritis because of the fenestrated vasculature structures resulting in the enhanced permeability and retention (EPR) effect. [4] These features allow nanoprobe systems to be more preferable for targeted delivery of drug or imaging agent. Second, the building blocks of nanoprobes (proteins, carbohydrates, nucleic acids, synthetic

polymers and small inorganic particles) are generally smaller than about several scores of nanometers. [5] Nanoprobes were fabricated by the assembly of these blocks for particular purpose. Therefore, it is inevitably determined that the scale of most nanoprobes is several scores or hundreds of nanometers. Third, nanoprobes have potential for wide applications due to easy containing of useful molecules such as imaging agents, active targeting moieties, or drugs by simple loading or conjugation. Once well-designed nanoprobe was developed and its feasibility was confirmed, it can be used to other purpose by small changes of containing functional molecules. [6] Thus, it is valuable that innovate design of nanoprobes for multiple targets and simple modification or improving for various purpose on both imaging and therapy. Moreover, target cell specificity can be equipped by simple conjugation of active targeting moieties like antibody or peptide. [7] Several nanoprobes can be degraded or dissembled to release their containing molecules at specific conditions, and some are based on the fluorescence quenching systems which can be activated at specific condition. [8] Moreover, simultaneous imaging and therapy are enabled, when both imaging molecules and drugs are adapted to same nanoprobe. [9]

Disease progress, inflammation, and therapeutic treatment can lead to some physiological and biochemical changes within human body microenvironment.

Thus, it is significantly valuable to know the exact site and the degree of changes in the biomedical perspective. To detect these changes in living systems, various smart nanoprobes were developed. [10]

1.1.2. Materials of Nanoprobe

The size-dependent tunable various properties of nanomaterials are fundamental to the excitement and wide applications. The most attractive nanomaterials are derived from silica, noble metals, semiconductors, lanthanides, metal oxides, polymers, and carbon. Among such nanomaterials, silica nanoparticles, gold nanoparticles, quantum clusters, semiconductor quantum dots, upconversion nanoparticles, polymer nanoparticles, carbon nanotubes, nanodiamonds, fullerenes, and graphene are subjects of fundamental research and biomedical technology. [11] Combinations among fluorescence, magnetic resonance, positron emission, photothermal and photoacoustic effects, surface plasmon, Raman and surface enhanced Raman scattering (SERS) presented by the above nanomaterials enable to resolve various problems in biology and medical science. Furthermore, the abilities of nanomaterials to accommodate multiple functional groups, targeting biomolecules, drugs, and genes allow one to use them for not only the detection of the structures and functioning of subcellular organelles and biomolecules but also the targeted imaging and treatment of various cancers. [11] Fabrication of colloidal nanoparticles with well-controlled size- and shape-distributions, well-defined surface chemistry, and unique

optical and electronic properties is the basis of all such biological applications of nanomaterials. The large surface to volume ratios of nanomaterials and their surface modifications using various chemical and bioconjugate reactions have moved the interface among chemistry, materials science and biology towards biomedical science. Recent research trends at this interface show focusing effects on the *in vitro* and *in vivo* applications of nanomaterials, such as multiplexed detections, biosensing, multimodal bioimaging, gene and drug delivery, and cancer chemotherapy and phototherapy (Figure 1). [11]

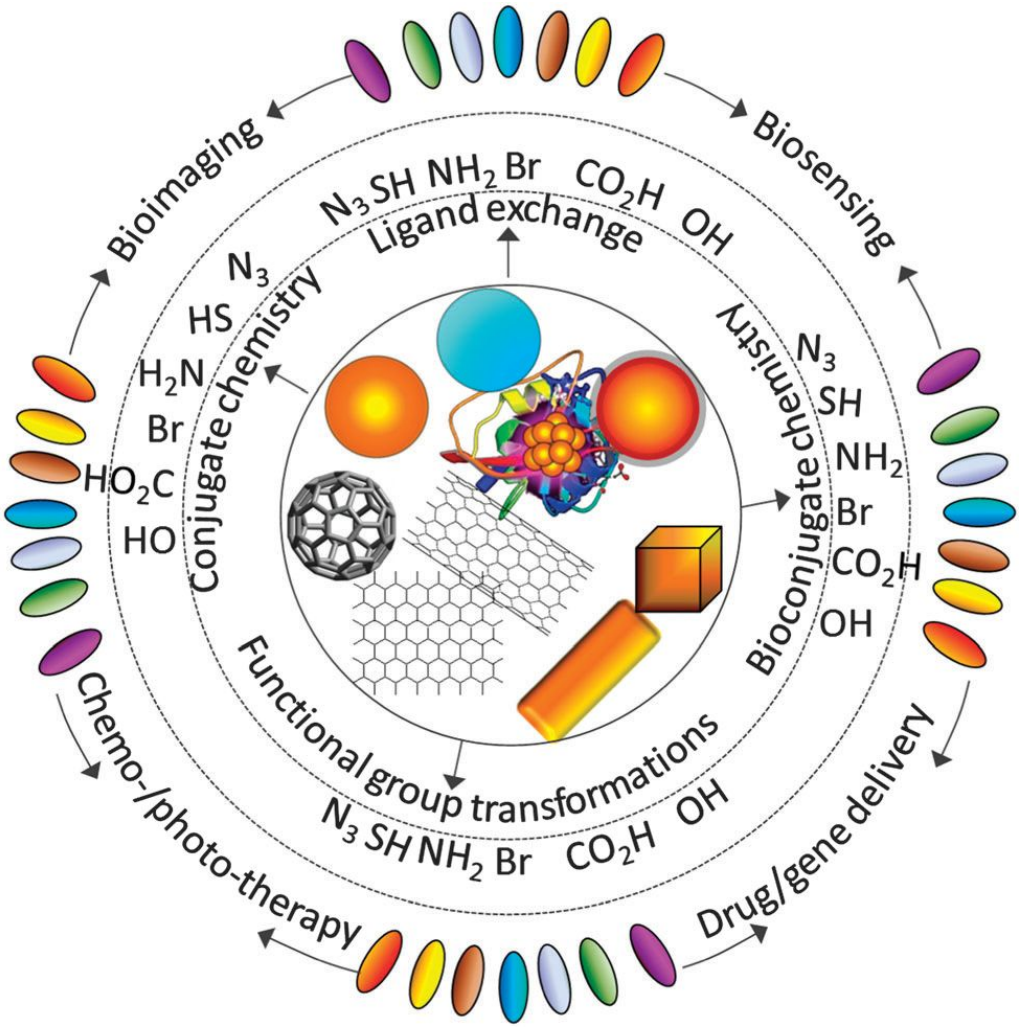

Figure 1. Examples of nanomaterials and their functional groups for biological applications. [11]

1.1.2.1. Polymer nanomaterials

Polymers are most general building blocks of nanoprobes due to their easily tunable characters. [12] Their physicochemical properties such as size, charge, hydrophobicity, branching and degradation can be controlled by changing their chemical structure or physical fabrication method. Various natural or synthetic polymers have been used for nanoprobe fabrication. Carbohydrates like hyaluronic acid, dextran, chitosan, pulluran and their derivatives can be adjusted to proper sizes and widely applied to the clinical fields. [12] Proteins such as albumin, transferrin, and antibodies are used as both building blocks and targeting moieties for nanoprobe development. [13] Recently, nucleic acids are also paid many attentions owing to its target specific binding ability. [14] In addition, biocompatible synthetic polymers such as polyetheyleneglycol (PEG), polyvinylpyrrolidone (PVP) and poly(lactic-co-glycolic acid) (PLGA) have approved for their biomedical applications to human body and usefully applied for many probes. [15]

1.1.2.2. Quantum dots nanomaterials

The semiconductor quantum dots are one of the most attractive nanomaterials in the photovoltaic, optoelectronic, electrooptical and biomedical fields. Their size-dependent tunable optical and electronic

properties make them attractive for various applications. Among the unique properties of quantum dots, broad absorption and narrow emission bands, large one- and two-photon absorption cross-sections, bright and stable photoluminescence and large surface area are attractive for the *in vitro* and *in vivo* detection or imaging. [11] Bioconjugated quantum dots have become regular parts of biology for sensing, gene and drug delivery, cell and biomolecular imaging, and photodynamic therapy experiments. Selected biological applications of quantum dot are shown in Figure. 2.

Quantum dots are extensively exploited in the construction of fluorescence- and FRET-based biosensors for the ultrasensitive detection of biomolecules such as nucleic acids, sugars, enzymes, antigens and antibodies. [16] One of the most interesting properties of quantum dots for biosensing is their narrow emission band, which allows for multiplexed detections of DNA strands or gene fragments in DNA finger printing, and antibodies or toxins in pathogen detections. The detection of glucose on quantum dot-based higher order structures and TNT using functionalized quantum dots are interesting biosensor applications. Quantum dots assembled with organic dyes such as fluorescein serve as FRET or fluorescence intensity-based ratiometric pH sensors. Quantum dots conjugated with various anticancer antibodies find applications such as the detection of cancer biomarkers in immunomicrochannels or

immunochromatographs. [11]

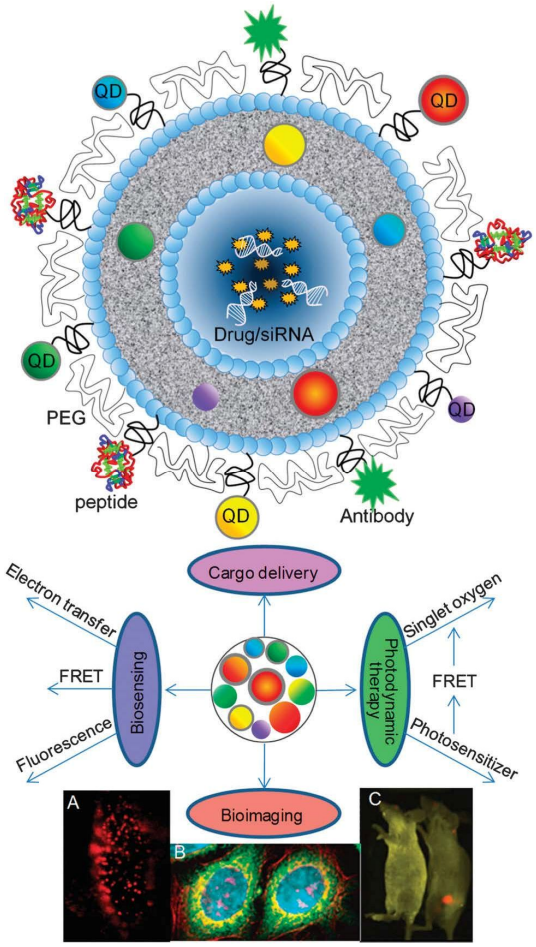

Figure 2. Biological applications of semiconductor quantum dots; (A) fluorescence image EGFR single-molecules in a A431 cell labeled using quantum dot-EGF conjugates, (B) pseudo-colored image showing five-color labeling of fixed human epithelial cells using quantum dot-bioconjugates, and (C) prostate tumor in a mouse labeled using quantum dot-PSMA antibody conjugate. [11]

1.1.2.3. Gold nanomaterials

Colloidal gold nanoparticles have been used as coloring agents for centuries. The brilliant color and size- and shape-dependent tunable surface plasmon of colloidal gold nanoparticles make them attractive for various applications such as solar energy harvesting, sensing, catalysis, bioimaging, drug delivery and photothermal cancer therapy. Optical and electronic properties of gold nanoparticles for such applications can be tuned by not only varying the size and shape but also their surface chemistry and aggregation state. [17] Several methods for the preparation of colloidal gold are recently introduced. [17-19] Photographs and absorption spectra of colloidal solutions of gold nanorods are shown in Figure 3. Subnanometer atomic clusters of gold and silver are promising candidates for biological applications. [20,21] Although these clusters were first detected in the gas phase, their biological applications have become possible only with the large scale preparation in the aqueous and organic phases. [22] Gold quantum clusters show broad absorption of light in the UV-Vis region and bright Vis-NIR photoluminescence (Figure 3D and E) due to the 'molecule-like' electronic transitions and the confinement of conduction electrons within the Fermi electron wavelength. Ligands such as bovine serum albumin (BSA), glutathione or alkane thiols are promising capping agents for the nanoclusters formed. The straight forward synthesis,

broad absorption spectra, size-dependent tunable photoluminescence color (Figure 3D), exceptional photostability, non-toxic nature and the ability to produce singlet oxygen make quantum clusters promising candidates for bioimaging and photodynamic therapy. [23] Surface plasmon resonance (SPR) of gold nanomaterials are extensively exploited in a lot of biological applications. Physicochemical properties of capping ligands and functional groups on gold play crucial roles in such applications. Successively, such surface modified gold nanoparticles become valuable sensors of DNA hybridization processes, protein–protein interactions, pathogens, cancer cells, antigens and various toxic materials. [24,25] These examples suggest that the functionalized gold nanoparticles are suitable for various biosensing applications.

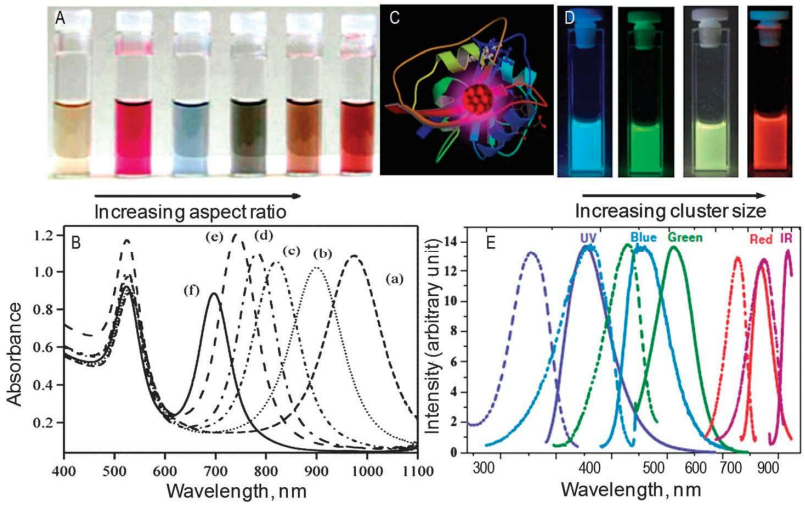

Figure 3. (A) Photograph of an aqueous solution of 4 nm gold nanospheres (left) and progressively higher aspect ratio gold nanorods. (B) UV-Visible absorption spectra of gold nanorods with different lengths (C) Au25 quantum cluster in BSA. (D) Photographs of polymer-coated gold quantum clusters having different size under UV excitation. (E) Absorption and photoluminescence spectra of UV (Au5), blue (Au8), green (Au13), red (Au23), and near IR (Au31) quantum clusters stabilized in PAMAM dendrimers. [11]

1.1.2.4. Silica nanomaterials

Silica nanoparticles can be classified into solid or non-porous and mesoporous. Silica nanoparticles have become common platforms for various catalytic/chemical reactions, bioimaging, and drug/gene delivery applications due to the straightforward, size-controlled synthesis, chemical/physical stabilities, large surface area, hydrophilic surface and well-defined surface chemistry. The same physico-chemical properties that make these materials ideal for the above applications also make them suitable as a protecting shell material for a spectrum of nanomaterials. Such silica shells not only render nanomaterials with hydrophilic, biocompatible and chemically active surfaces but also protect them against chemical and biochemical degradations, release of toxic ions, and activation of immune response. The Stöber process, which is the controlled hydrolysis of silyl ethers such as tetraethyl silicate into silanols using ammonia in a mixture of water and alcohol followed by the condensation of silanols into 50–2000 nm silica particles, is the basis of silica nanoparticle preparation. In this preparation, the size of silica particles can be controlled by either varying the concentrations of silyl ether and alcohol, or the normal or reverse microemulsion method, which are modifications of the Sto¨ber process. [25] The reverse microemulsion method is the ammoniacatalyzed polymerization of silyl ethers loaded in a microemulsion. Mesoporous silica

nanoparticles are synthesized by the sol–gel process, which is the in situ polymerization of silyl ethers stabilized in amphiphilic templates provided by surfactants such as cetyltrimethylammonium bromide (CTAB). [26] Aggregation of silica nanoparticles during the synthesis can be prevented by setting the concentration of silyl ether at a low level or by the addition of non-ionic surfactants, polymers, triethanolamine or propanetriol. Finally, the templates are removed by solvent extraction, thermal decomposition, dialysis or oxidation. The pore-size of mesoporous silica nanoparticles thus synthesized can be controlled by varying the pH of the solution and composition of the solvents, and the addition of certain swelling agents.

As-synthesized silica nanoparticles by the standard procedures discussed above own highly hydrophilic surfaces, which make them one of the friendliest nanomaterials for biomedical applications such as drug and gene delivery, bioimaging and therapy. However, assorted surface functional groups are often necessary for the conjugation of various biomolecules, contrast agents and drugs to the surface as well as inside the pores of silica nanoparticles. Reactive functional groups such as a primary or a secondary amino, carboxyl, hydroxyl, alkyl halogen, or azide group can be introduced onto the surface of silica nanoparticles by either the co-condensation process during the preparation or by postsynthesis surface modification. [25] Although co-condensation provides

uniform distribution of such functional groups, postsynthesis surface modification is preferable for maintaining the size-distribution and morphology of silica nanoparticles during the synthesis. In post-synthesis surface modifications (Figure 4), various trialkoxysilanes are condensed with the surface silanol group. 3-Aminopropyl tri(m)ethoxy silane and 3-mercaptopropyl tri(m)ethoxy silane are extensively employed in such condensation reactions, which provide primary amine and thiol groups on the surface of silica nanoparticles. [26] The direct condensation of silane-functionalized molecules such as organic dyes, polyethylene glycol (PEG), etc. to the silanol group on as-synthesized silica nanoparticles can also be practiced. [27] Amino-functionalized silica nanoparticles can be conjugated with other nanoparticles, small organic molecules, proteins, peptides, nucleic acids, fluorescent dyes, etc. by coupling with functional moieties such as carboxylic acids, alkyl halides and NHS esters. These reactions are summarized in Figure 4. Common coupling agents commercially available for such reactions are 1-ethyl-3-(3-dimethylaminopropyl) carbodiimide (EDC), diisopropyl carbodiimide (DIC), N-hydroxysuccinimide (NHS) esters, [N,N,N0,N0-tetramethyl-O-(1H-benzotriazol-1-yl)uronium hexafluorophosphate] (HBTU), (N-succinimidyl 3-[2-pyridyldithio]-propionate) (SPDP) and sulfosuccinimidyl-(4-N-maleimidomethyl)cyclohexane-1-carboxylate (sulfo-

SMCC). [27] Here, the succinimidyl group in the heterobifunctional cross-linkers such as SPDP and sulfo-SMCC reacts with the amino group on silica; whereas, the pyridyldithio and maleimide moieties can be utilized for the conjugation of sulfhydryl groups in thiols and cysteine-bearing proteins. Primary amino groups on silica nanoparticles can also be coupled with aldehydes and ketones to form Schiff's bases, isothiocyanates to form thiourea derivatives, or metal complexes to form chelate bonds. Reactions of surface amino groups on silica with Wilkinson's catalyst and cisplastin are typical examples for chelate bond formation. Isothiocyanates of rhodamine and fluorescein are commercially available agents for the direct fluorescence labeling of amino-functionalized silica nanoparticles. As-synthesized silica nanoparticles are abundant in hydroxyl groups, which can be conjugated with isocyanates to form urethanes or carboxylic acids to form esters. The condensation of 3-mercaptopropyltriethoxy silane or its analogues with silanol groups on the surface of silica nanoparticles offers thiol functionalized silica nanoparticles, which can be further conjugated with gold nanoparticles, proteins, antibodies, peptides, fluorophores, polymers, etc. by reductive addition, disulfide coupling or maleimide reaction. Thiol functionalized molecules react with thiol groups on the surface of silica nanoparticles to form

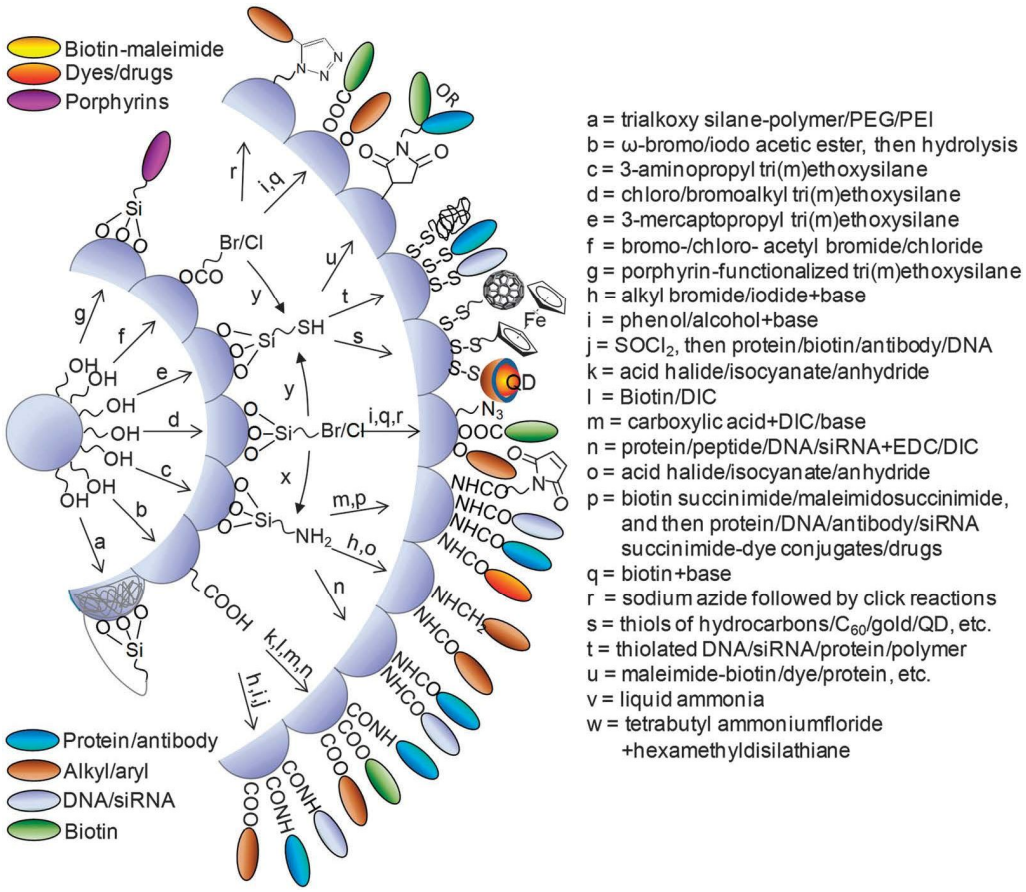

Figure 4. Common methods for the functionalization and bioconjugation of silica nanoparticles. [11]

redox-active disulfide bonds, which are candidates of redox-sensitive drug delivery systems. [28] Similarly, maleimidefunctionalized molecules react with thiol groups on the surface of silica nanoparticles to form stable thioether bonds. Introduction of azide groups and the subsequent click chemistry with alkyne substituted molecules is also a versatile method for the functionalization of silica nanoparticles. Other common methods for the functionalization of silica nanoparticles include polymerization by the attachment of functional groups suitable for chain transfer or free radical polymerization. Common methods for the chemical and bioconjugate reactions of silica nanoparticles are summarized in Figure 4.

1.1.3. Fluorescent Nanoprobe for Bioimaging applications

The application of nanomaterials in biomedical imaging is highly active and exciting for wide range of targets for imaging. [29-31] The impact of nanomaterials improves the efficacy of conventional imaging moieties and make entirely new imaging methods. [32] A lot of challenging developments and clinical applications of novel nanomaterials have been developed with the help of nanotechnology. [33,34] Among various applications of nanomaterials for biomedical imaging such as cell tracking, diagnostic kit, harvested tissue analysis, and live imaging, the present article aims to describe about the real-time live imaging with nanoprobes and detecting particular changes of microenvironments in living systems.

1.1.3.1. ROS sensing

Reactive oxygen species (ROS), including hydrogen peroxide (H_2O_2), hydroxyl radicals, superoxide anion radicals and singlet oxygen, are highly reactive molecules, which are produced by cellular metabolism. As a major ROS in living systems, H_2O_2 plays a key role as a second messenger in normal cellular signal transduction. In living systems, the involvement of H_2O_2 in cellular signaling and disease states has motivated the development of chemical tools that can be employed to understand how cells produce and funnel H_2O_2

into specific signaling pathways. Fluorescent imaging with H_2O_2-responsive NIR fluorophores creates a unique opportunity for real-time, noninvasive detection of H_2O_2 in biological specimens. Currently, boronate-based fluorescent probes have been widely employed to detect intracellular H_2O_2. The operation of boronate-based NIR probes takes advantage of the fact that aryl boronates are selectively oxidatively transformed to the corresponding phenols by H_2O_2. Recently, cyanine-based fluorescent probe 1 was exploited for sensing H_2O_2 which contains boronate as a specific reactive moiety. (Figure 5a). [35] The boronate-masked phenol group causes 1 to possess a reduced conjugated p-electron system. Thus, in the absence of H_2O_2, probe 1 displays almost no fluorescence in aqueous solutions. In contrast, H_2O_2-promoted transformation of the boronate group in 1 to a phenol group results in generation of an extensively conjugated p-electron system that emits a strong NIR fluorescence signal. This probe was demonstrated to be effective for imaging endogenous H_2O_2 produced in an acute inflammation mouse model (Figure 5b).

1.1.3.2. Thiol sensing

Intracellular thiol-containing molecules (cysteine, homocysteine, and glutathione) play essential roles in maintaining the redox homeostasis of

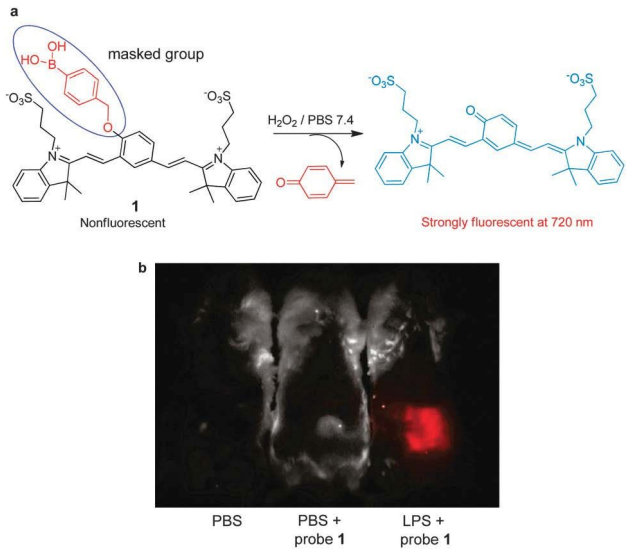

Figure 5. (a) A mechanism for sensing hydrogen peroxide by 1; (b) detection of endogenous hydrogen peroxide produced in a mouse during a lipopolysaccharide (LPS)-induced inflammatory response, using 1. [30]

protein, cells and organisms. Abnormal levels of these molecules lead to detrimental effects, such as slow growth, liver damage and skin lesions, on human health. Recently, the ratiometric fluorescent probe 2 for selective detection of cysteine (Cys) was developed (Figure 6). [36] In probe 2, an acrylate group serves as the thiol specific trigger moiety. The results show that probe 2 displays a colorimetric and ratiometric response to Cys. In addition, the probe has an excellent selectivity for Cys over homocysteine (Hcy) and glutathione (GSH) due to the greatly different rates of the intramolecular cyclization process that produces the cyclohexanone containing product. The probe was utilized for bioimaging Cys in breast cancer cells.

1.1.3.3. Ion sensing

Copper is an essential transition metal in living organisms because it is involved in various physiological processes such as enzyme catalysis, development and growth. Loss of copper homeostasis in an organism results in neurodegenerative diseases including Alzheimer's disease, Menkes disease (copper deficiency), Wilson's disease (copper overload) and amyotropic lateral sclerosis. Despite the biological significance of copper ions, only a few fluorescent probes have been exploited for their detection. The fluorescent probe 3 was composed of tricarbocyanine as a fluorophore and 2,20-azanediyl

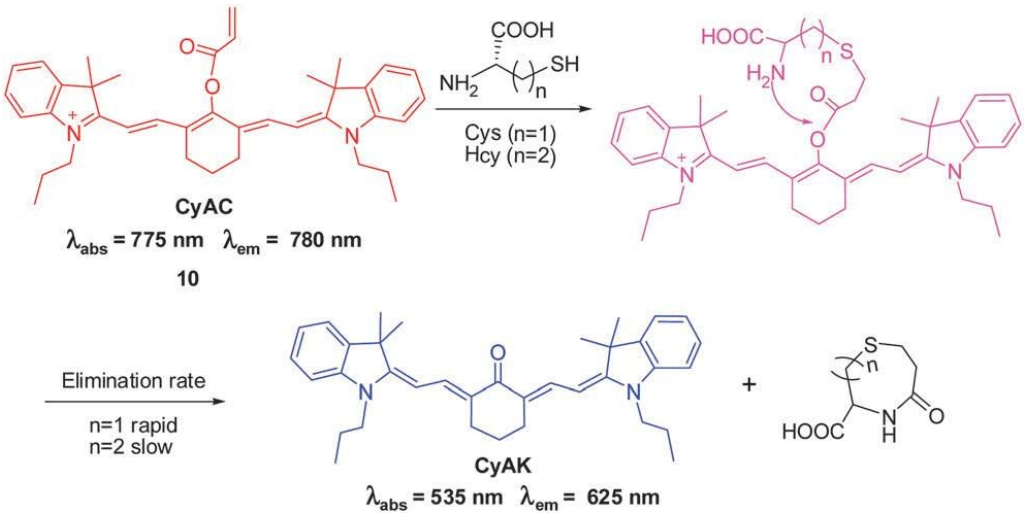

Figure 6. A proposed mechanism for sensing Cys by 2. [30]

bis(N-hydroxyacetamide) as a Cu^{2+} receptor, for detection of Cu^{2+} (Figure 7). [37] Its fluorescence is strongly enhanced upon binding to Cu^{2+}, which blocks PET quenching, while free 3 displays weak fluorescence because of a PET quenching mechanism. Probe 3, which has good selectivity toward Cu^{2+} over other biologically relevant cations, has been employed to image exogenous Cu^{2+} in living cells.

Among toxic metal ions, mercury is one of the most prevalent on earth. Mercury species in the body cause damage mainly to the central nervous system. Concern over the toxicity of mercury has stimulated the development of selective and efficient methods to sense mercury ions in cells and organisms. Although many fluorescent probes have been developed for this purpose, mercury-selective fluorescent probes have been only recently described. The fluorescent probes 4 and 5 to monitor Hg^{2+} and CH_3Hg^+ were based tricarbocyanine (Figure 8). [38] These probes show a great selectivity to Hg^{2+} over other metal ions. The results of cell experiments reveal that probes 4 and 5 can be applied to the monitoring of mercury ions in cells.

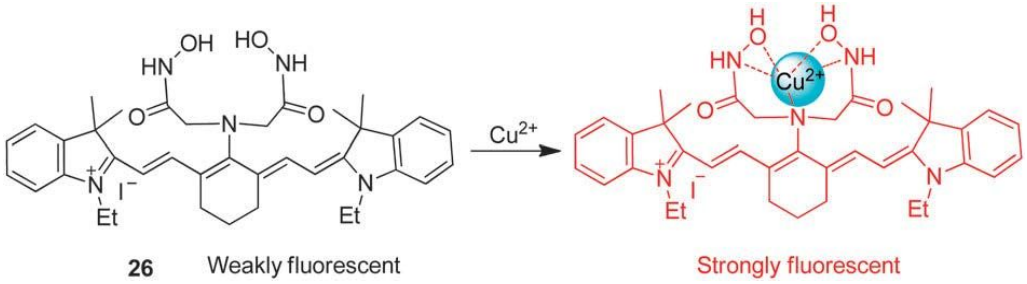

Figure 7. A proposed mechanism for sensing Cu^{2+} by 3. [30]

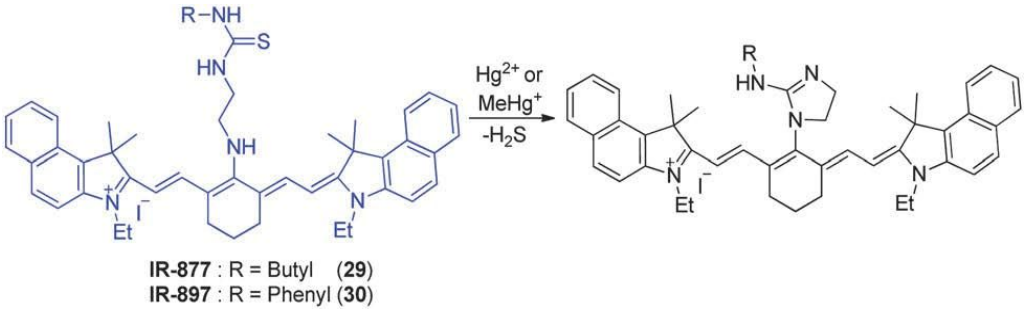

Figure 8. A proposed mechanism for sensing Hg^{2+} or $MeHg^{+}$ by 4 and 5. [30]

1.2. Objectives and Outlines

1.2.1 Objectives

The aim of this dissertation is to provide synthetic methodologies to fabricate the various fluorescent nanomateirals and evaluating their properties as nanoprobe. In particular, two types of polyacrylonitrile (PAN) nanoparticle based fluorescent nanoprobe and graphene quantum dots (GQDs) are fabricated by chemical reduction and sonication mediated methods. In case of polymer based fluorescence probe, polyacrylonitrile (PAN) nanoparticle was modified with dual amidine/Schiff base for detecting intracellular copper ions. Gold nanocluster also decorated on the PAN nanoparticles and graphene quantum dost (GQDs) for fluorescence probe for sensing mercury ion and cysteine, respectively. Each hybrid nanoprobe is deliberately designed and customized for superior performance in detecting applications.

1.2.2. Outline

This dissertation involves the following subtopics:

I. Amidine/Schiff Base Dual-Modified PAN Nanoparticles and Their Application
   1. Fabrication of Amidine/Schiff Base Dual-Modified PAN Nanoparticles
   2. Application for Intracellular Copper Ion Detection

II. Au-decorated PAN Nanoparticles with Dual-Emission and Their Application

1. Fabrication of Au-decorated PAN Nanoparticles with Dual-Emission
2. Application for Mercury Ion Detection

III. Au-decorated Graphene Quantum Dots with Dual-Emission and Their Application

1. Fabrication of Au-decorated Graphene Quantum Dots with Dual-Emission
2. Application for Intracellular Cysteine Detection

A detailed outline of the study is as follows:

1. Highly fluorescent surface modified polyacrylonitrile nanoparticles (PAN NPs) of 50 nm diameter were fabricated for selective copper ion sensing. After surface modification of PAN nanoparticles, the PAN nanoparticles are converted to amidine/Schiff base dual-modified PAN nanoparticles (tPAN NPs) with a copper ion sensing property and high QY (0.19). The selectivity of tPAN NPs for copper ion is much higher than other metal ions due to the fact that amidine group on the surface of tPAN NPs have a higher binding affinity with copper ion. The effect of other metal ions on the fluorescence intensity of tPAN NPs was also studied and other metal

ions showed low interference response in detection of copper ion. Furthermore, as a metal ion chelator, ethylenediaminetetraacetate can competitively interact with copper ion to recover the quenched fluorescence of tPAN NPs. The tPAN NPs are easily introduced into cells and exhibit low toxicity enabling their use as a fluorescence sensor for copper ion in living cells. The tPAN NPs provide a new direction for the development of copper ion sensors in living cells.

2. A dual-emission probe of an Au nanocluster-PAN nanocomposite developed for detection of mercury ions. For the capability to detect Hg(II) ion selectively, the surface of the gold nanoparticle was modified with mercaptopropionic acid (MPA) and homocystine (bound to the gold nanoparticle surface through a Au-S bond). The properties of Au-PAN NPs can be used for rapid, easy and reliable screening of Hg(II) ions in aqueous solution, with high sensitivity (1 nM) and selectivity over competing analytes. The results show that the monitoring Hg(II) ions using Au-PAN NPs has excellent selectivity over other metal ions
3. The graphene quantum dots (GQDs) were used as fluorescence probe for detecting intracellular cysteine. Orange fluorescent gold nanocluster, fabricated by chemical reduction method, was decorated on the GQDs. Folic acid added to enhance interacting with target cells. Among various

targeting system, the folic acid was selected as model targeting agent for enhancing internalization and selectivity of cancer cells. The Au decorated GQDs were further applied as dual emission fluorescence probe for monitoring intracellular highly cysteine.

2. EXPERIMENTAL DETAILS

2.1. Amidine/Schiff Base Dual-Modified PAN Nanoparticles and Their Application

2.1.1. Fabrication of Amidine/Schiff Base Dual-Modified PAN Nanoparticles

The Hydrogen chloride and diethyl ether were purchased from Samchun Chemical. The following chemicals purchased from Aldrich: acrylonitrile monomer, dodecylsulfate, cerium sulphate, nitroacetic acid, ammonia solution, ethylenediaminetetraacetate, $Al(NO_3)_3$, $AgNO_3$, $CdCl_2$, $CoCl_2$, $CuCl_2$, $FeCl_3$, $FeCl_2$, $HgCl_2$, $MgCl_2$, $MnCl_2$, $NiCl_2$, $Pb(NO_3)_2$, ZnCl2, NaCl, KCl, and $CaCl_2$.

The PAN NPs of 50 nm sizes were fabricated by microemulsion polymerization. To fabricate PAN nanoparticles, acrylonitrile (AN; 1.5 g) monomer was dissolved in distilled water with 0.5 g sodium dodecyl sulfate (SDS). After introducing cerium sulphate and nitroacetic acid, the microemulsion polymerization of the AN monomer proceeded for 10 min. The resulting product was washed with ethanol in 3 times.

The surface-treated PAN nanoparticles (tPAN) were achieved by surface modification. This was followed by treatment with hydrogen chloride and then ammonia under nitrogen to form amidine and Schiff base groups on the PAN nanoparticles. First, a 0.5 g amount of PAN nanoparticles in ethanol (10 mL)

was added into 1 M HCl in diethyl ether (20 mL) at 0 °C for 72 h in round-bottomed flasks under N_2 reflux. Then, the product was washed with ethanol. The product was treated with ammonia solution (20 mL) under a nitrogen purge for 3 h. The product was washed with ethanol in 3 times.

The transmission electron microscope and scanning electron microscope images were taken with a JEOL JEM-2100 and JEOL 6330F, respectively. FT-IR spectra were collected with a Thermo Scientific Nicolet 6700 FTIR spectrophotometer. The samples for IR detection were prepared by potassium bromide (KBr) pellet method. The powder sample grounded with KBr was pressed to form a pellet. The pellet samples were investigated by IR spectroscopy transmission mode. The fluorescent emission spectra of tPAN nanoparticles were obtained with a JASCO FP-6500 spectrofluorometer.

The quantum yield of tPAN particles was obtained by comparing between the fluorescence emission of reference dye and that of tPAN nanoparticles. 7-amino-4-methylcoumarin is blue-emitting dye with high quantum yield (Φ = 0.88), which is used as standard reference. The quantum yield of tPAN particles was calculated by the following equation:

$$\Phi_P = \frac{F_P}{A_P} \times \frac{A_D}{F_D} \times \Phi_D$$

where Φ is the fluorescence quantum yield, F is the integrated area of

emitted fluorescence spectra, and A is the absorbance at the excitation wavelength. The subscript P and D implied tPAN particles and 7-amino-4-methylcoumarin, respectively.

2.1.2. Application for Intracellular Copper Ion Detection

Human breast cancer SK-BR-3 cells (American Type Culture Collection, Manassas, VA, USA) were cultured in RPMI-1640 medium with 10 % fetal bovine serum and 1 % penicillin-streptomycin solution. They were maintained in a 75T flask at 37 °C in humidified 5 % CO_2 atmosphere and passaged at 70-80 % confluence.

SK-BR-3 cells were seeded at a density of 3000 cells per well, in 8-well Lab-Tek II chambered coverglass (Nunc, Thermo Fisher Scientific, USA) and inserted with 10 μg mL^{-1} of tPAN NPs. After 24 h, the cells were washed twice with 0.1 M phosphate buffered solution (PBS), and treated with 10 μM $CuCl_2$ for 20 min at 37 °C. As control experiment, excess ethylenediaminetetraacetate (EDTA, 100 μM) was incubated for 20 min to remove Cu^{2+} from the culture medium. The cells were washed again and analyzed with a Delta Vision RT imaging system (Applied Precision, Issaquah, WA, USA). To obtain images, a Cascade II electron multiplying charge-coupled device camera was used.

For cell viability, Cell-Titer glow luminescent cell viability assay (Promega, Madison, WI, USA) was used. SK-BR-3 cells were seeded in white opaque 96-well plates at a density of 1.5×104 cells mL^{-1} for 24 h, and various concentration of tPAN NPs (5, 10, 50, 100, and 250 μg mL-1) were inserted for another 24 h. Then, culture medium was eliminated and following steps were

performed by manufacturer's instructions. The luminescence (595 nm) was detected by Victor3 Multilabel Readers (Perkin Elmer, Boston, MA, USA). The viability was calculated by dividing the ATP content of tPAN NPs-treated cells by that of untreated cells (negative control).

For the measurement of ROS, 2',7'-dichlorodihydrofluorescein diacetate (H2DCF-DA; Invitrogen, Grand Island, NY, USA) staining was performed. SK-BR-3 cells were spread in black opaque 96-well plates at a concentration of 1.5×104 cells mL^{-1} for 24 h, and treated with tPAN NPs (5, 10, 50, 100, and 250 μg mL^{-1}) for another 24 h. They were washed with 0.1 M Hank's Buffered Salt Solution and treated with 10 μM H2DCF-DA for 30 min at 37 °C. Fluorescence intensity was detected by Victor3 Multilabel Readers (λ_{ex}=485 nm, λ_{em}=535 nm).

2.2. Au-decorated PAN Nanoparticles with Dual-Emission and Their Application

2.2.1. Fabrication of Au-decorated PAN Nanoparticles with Dual-Emission

The Hydrogen chloride and diethyl ether were purchased from Samchun Chemical. The acrylonitrile monomer, dodecylsulfacte, cerium sulphate, nitroacetic acid, ammonia solution, ethylenediaminetetraacetate, L-glutathione, $HAuCl_4$, $NaBH_4$, $Al(NO_3)_3$, $AgNO_3$, $CdCl_2$, $CoCl_2$, $CuCl_2$, $FeCl_3$, $FeCl_2$, $HgCl_2$, $MgCl_2$, $MnCl_2$, $NiCl_2$, $Pb(NO_3)_2$, $ZnCl_2$, NaCl, KCl, and $CaCl_2$ were purchased from Sigma Aldrich.

The PAN NPs of 50 nm sizes were fabricated by microemulsion polymerization. To fabricate PAN nanoparticles, acrylonitrile (AN; 1.5 g) monomer was dissolved in distilled water with 0.5 g sodium dodecyl sulfate (SDS). After introducing cerium sulphate and nitroacetic acid, the microemulsion polymerization of the AN monomer proceeded for 10 min. The resulting product was washed with ethanol in 3 times.

The tPAN nanoparticles were achieved by surface modification. This was followed by treatment with hydrogen chloride and then ammonia under nitrogen to form amidine and Schiff base groups on the PAN nanoparticles. First, a 0.5 g amount of PAN nanoparticles in ethanol (10 mL) was added into

1 M HCl in diethyl ether (20 mL) at 0 °C for 72 h in round-bottomed flasks under N_2 reflux. Then, the product was washed with ethanol. The product was treated with ammonia solution (20 mL) under a nitrogen purge for 3 h. The product was washed with ethanol in 3 times.

The gold nanocluster (AuNCs) were synthesized by reduvtion of $HAuCl_4$ with L-glutathione (GSH). According to the prvious report, GSH aqueous solution (6 mM, 10 mL) was mixed with $HAuCl_4$ aqueous solution (4 mM, 10 mL) under srtirred condition at 90 for 6.5 h. [39] To prepare Au-tPAN NPs, AuNCs (2 mg mL^{-1}, 40 mL) were mixed with 300 mg mL^{-1} of 1-ethyl-3-(3-dimethylaminopropyl)-carbodiimide (EDC) for 15 min. tPAN NPs (50 mg mL^{-1}, 1 mL) aqueous solution was reacted with 300 mg mL^{-1} of N-hydroxysuccinimide (NHS) for 15 min. Then, tPAN NPs, which are activated by N-hydroxysuccinimide, were poured into the solution containing AuNCs and 1-ethyl-3-(3-dimethylaminopropyl)-carbodiimide, and reacted with vigorous stirring for another 2 h. Resulting Au-tPAN NPs were washed with distilled water and centrifugation.

To detect Hg(II) ion selectively, the surface of the gold nanoparticle was modified with mercaptopropionic acid (MPA) and homocystine (Hcy; bound to the gold nanoparticle surface through a Au-S bond). The gold nanoparticle surface was attached with MPA and Hcy through a -SH bond. 10 mM MPA

(10 μL) and 2 mM Hcy (10 μL) were added to the gold nanoparticle solution (15 nM, 10 mL) with stirring. After 2 h, 5 mM $NaBH_4$ was added, and the mixture was left for few hours without disturbance.

The transmission electron microscope and scanning electron microscope images were taken with a JEOL JEM-2100 and JEOL 6330F, respectively. FT-IR spectra were collected with a Thermo Scientific Nicolet 6700 FTIR spectrophotometer. The samples for IR detection were prepared by potassium bromide (KBr) pellet method. The powder sample grounded with KBr was pressed to form a pellet. The pellet samples were investigated by IR spectroscopy transmission mode. The fluorescent emission spectra of tPAN nanoparticles were obtained with a JASCO FP-6500 spectrofluorometer.

2.2.2. Application for Mercury Ion Detection

The fluorescent emission spectra of Au-tPAN nanoparticles were obtained with a JASCO FP-6500 spectrofluorometer.

The quantum yield of tPAN particles was obtained by comparing between the fluorescence emission of reference dye and that of tPAN nanoparticles. 7-amino-4-methylcoumarin is blue-emitting dye with high quantum yield (Φ = 0.88), which is used as standard reference. The quantum yield of tPAN particles was calculated by the following equation:

$$\Phi_P = \frac{F_P}{A_P} \times \frac{A_D}{F_D} \times \Phi_D$$

where Φ is the fluorescence quantum yield, F is the integrated area of emitted fluorescence spectra, and A is the absorbance at the excitation wavelength. The subscript P and D implied tPAN particles and 7-amino-4-methylcoumarin, respectively.

2.3. Au-decorated Graphene Quantum Dots with Dual-Emission and Their Application

2.3.1. Fabrication of Au-decorated Graphene Quantum Dots with Dual-Emission

The Hydrogen chloride and diethyl ether were purchased from Samchun Chemical. The L-glutathione, $HAuCl_4$, cysteine and other amino acids were purchased from Sigma Aldrich

To obtain GQDs, HCNFs with diameters of 50–100 nm were used as the starting material. The small domain structure of sp^2 carbon atoms, such as those in carbon nanofibers (CNFs), has advantages of easy extraction and facile size control of the synthesized GQDs. The HCNFs were oxidized under excessive acidic conditions for 24 h and exfoliated to nanometer-sized graphene oxides. The oxidation process was carried out at temperatures ranging from 80 to 120 °C to synthesize GQDs. Then, the pH of the solution was adjusted to 8 using Na_2CO_3. To enhance the PL intensities of GQDs by surface passivation, the surface edges of graphene oxide sheets were anchored with polyethylene glycol (PEG, MW: 10000). The anchoring process was performed at 120 °C for 1 h *via* a hydrothermal method. Then, size-selective precipitation was used to isolate the GQDs from the reaction mixture. Ethanol, a non-solvent, was added to the concentrated solution until the Na_2SO_4 salts

started to precipitate. Excess Na^+ and SO_4^{2-} ions were present in the GQD solution due to the neutralization reaction between H_2SO_4 and Na_2CO_3; the excess ions combined to form Na_2SO_4 salts in a non-solvent system. From the resulting turbid solution, the precipitate and the supernatant were perfectly separated by centrifugation. Consequently, uniform nanometer-sized GQDs were separated from Na_2SO_4 salts and larger GQDs under various sedimentation velocity conditions

The gold nanocluster (AuNCs) were synthesized by reduvtion of $HAuCl_4$ with L-glutathione (GSH). According to the prvious report, GSH aqueous solution (6 mM, 10 mL) was mixed with $HAuCl_4$ aqueous solution (4 mM, 10 mL) under srtirred condition at 90 for 6.5 h. [39] To prepare Au-GQDs, AuNCs (2 mg mL^{-1}, 40 mL) were mixed with 300 mg mL^{-1} of EDC for 15 min. GQDs (50 mg mL-1, 1 mL) aqueous solution was reacted with 300 mg mL^{-1} of NHS for 15 min. Then, GQDs, which are activated by N-hydroxysuccinimide, were poured into the solution containing AuNCs and 1-ethyl-3-(3-dimethylaminopropyl)-carbodiimide, and reacted with vigorous stirring for another 2 h. Resulting Au-GQD NPs were washed with distilled water and centrifugation.

The transmission electron microscope and scanning electron microscope images were taken with a JEOL JEM-2100 and JEOL 6330F, respectively.

XPS spectra were collected with a SIGMA PROBE. Fluorescent emission spectra of GQDs nanoparticles were obtained with a JASCO FP-6500 spectrofluorometer.

2.3.2. Application for Intracellular Cysteine Detection

Human breast cancer MCF-7 cells (FR+) and human breast cancer SK-BR-3 cells (FR-) were purchased from American Type Culture Collection (Manassas, VA, USA). Both cells were cultured in RPMI-1640 medium with 10% fetal bovine serum and 1 % penicillin-streptomycin solution. They were maintained in a 75T flask at 37 °C in humidified 5 % CO_2 atmosphere and passaged at 70-80 % confluence.

Human breast cancer SK-BR-3 cells (American Type Culture Collection, Manassas, VA, USA) were cultured in RPMI-1640 medium with 10 % fetal bovine serum and 1 % penicillin-streptomycin solution. They were maintained in a 75T flask at 37 °C in humidified 5 % CO_2 atmosphere and passaged at 70-80 % confluence.

MCF-7 and SK-BR-3 cells were spread at a density of 3000 cells per well, in 8-well Lab-Tek II chambered coverglass (Nunc, Thermo Fisher Scientific, USA) and treated with 10 μg mL^{-1} of Au-GQDs. After 24 h, the supernatant was removed and the cells were washed twice with 0.1 M phosphate buffered solution (PBS). The cells were analyzed with a Delta Vision RT imaging system (Applied Precision, Issaquah, WA, USA) under 5 % CO_2 at 37 °C. To obtain images, a Cascade II electron multiplying charge-coupled device camera was used. The excitation and emission filter were used as Rd-TR-PE and DAPI,

respectively, to restriction of the fluorescence lamp of the instruments.

For cell viability, Cell-Titer glow luminescent cell viability assay (Promega, Madison, WI, USA) was used. MCF-7 cells were seeded in white opaque 96-well plates at a density of 1.5×104 cells mL-1 for 24 h, and various concentration of Au-GQDs (5, 10, 50, 100, and 250 μg mL^{-1}) were inserted for another 24 h. Then, culture medium was eliminated and following steps were performed by manufacturer's instructions. The luminescence (595 nm) was detected by Victor3 Multilabel Readers (Perkin Elmer, Boston, MA, USA). The viability was calculated by dividing the ATP content of Au-GQDs-treated cells by that of untreated cells (negative control).

For the measurement of ROS, 2',7'-dichlorodihydrofluorescein diacetate (H2DCF-DA; Invitrogen, Grand Island, NY, USA) staining was performed. MCF-7 cells were spread in black opaque 96-well plates at a concentration of 1.5×104 cells mL-1 for 24 h, and treated with Au-GQDs (5, 10, 50, 100, and 250 μg mL^{-1}) for another 24 h. They were washed with 0.1 M Hank's Buffered Salt Solution and treated with 10 μM H2DCF-DA for 30 min at 37 °C. Fluorescence intensity was detected by Victor3 Multilabel Readers (λ_{ex}=485 nm, λ_{em}=535 nm).

3. RESULTS AND DISCUSSION

3.1. Amidine/Schiff Base Dual-Modified PAN Nanoparticles and Their Application

3.1.1. Fabrication of Amidine/Schiff Base Dual-Modified PAN Nanoparticles

PAN NPs were fabricated by ultrasonic mediated emulsion polymerization, as reported previously. [40] Ultrasonic irradiation formed emulsion phase by dissolving sodium dodecylsulfate and acrylonitrile monomer in distilled water. After introducing cerium sulphate and nitroacetic acid, as co-initiators, into the solution, additional ultrasound was administered for polymerization of acrylonitrile monomer. In Figure 9, as-prepared PAN NPs were modified by hydrogen chloride and ammonia under nitrogen purge. Fabrication of the PAN NPs and their surface modification do not require complicated procedure and careful regulation of temperature as opposed to the preparation of QDs. [40-43] Due to change of the surface functional group, tPAN NPs can detect copper ions by amidine group and Schiff base has a role to enhance the fluorescence of tPAN NPs. The PAN and tPAN NPs had a narrow size distribution, largely in the range of 40-50 nm as determined by transmission electron microscope (TEM) and scanning electron microscope (SEM) images (Figure 10). Furthermore, high-resolution TEM (HRTEM) images (Figure 11) showed that

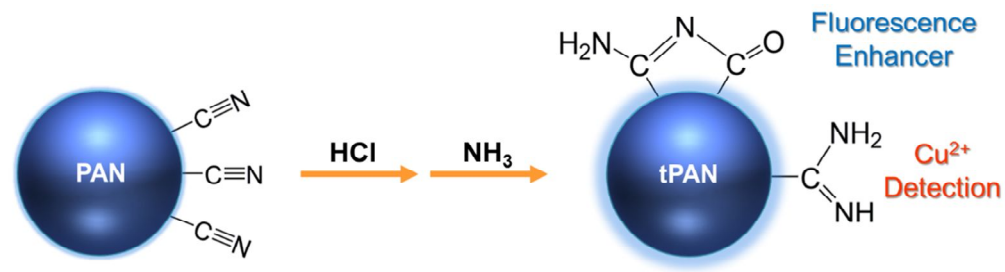

Figure 9. Schematic diagram of fabrication of tPAN NPs.

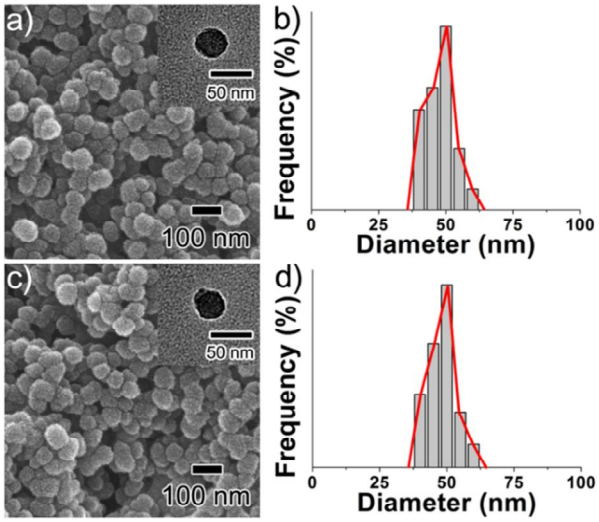

Figure 10. SEM images (inset: TEM images) and size distribution histograms of (a, b) PAN NPs and (c, d) tPAN NPs.

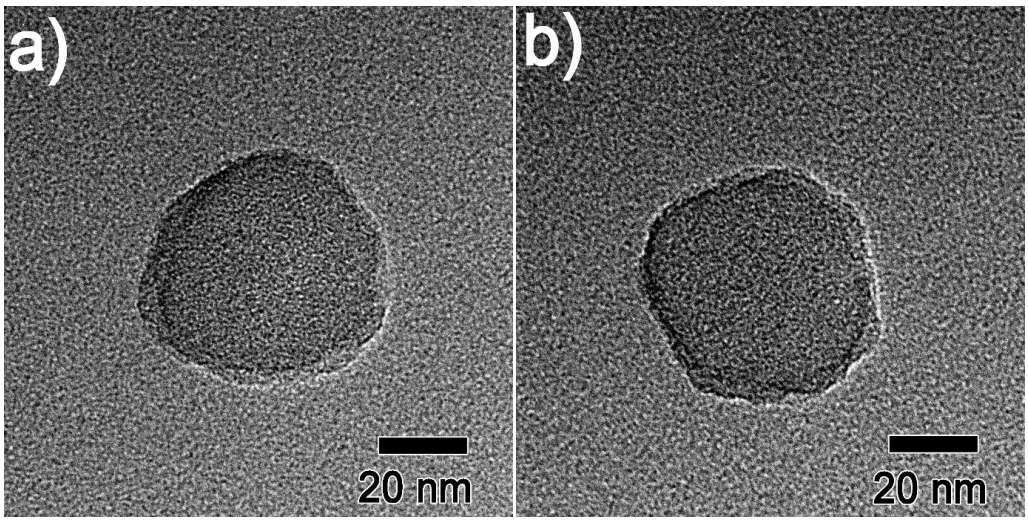

Figure 11. The HRTEM images of (a) PAN NPs and (b) tPAN NPs. The high-resolution TEM (HRTEM) images showed that the shape and size of PAN NPs and tPAN NPs were still maintained after surface modification.

the shape and size of PAN NPs and tPAN NPs were still maintained after surface modification.

Formation of the PAN NPs and the tPAN NPs was confirmed by Fourier-transform infrared (FT-IR) spectrometry (Figure 12). FT-IR spectrum of the PAN NPs showed characteristic PAN peaks, including the C≡N stretching bands at 2244 cm^{-1}, the C-H stretching peak at 2948 cm^{-1}, and C-H deformation peak at 1451 cm^{-1}. These peaks revealed successful polymerization of the PAN NPs by ultrasonic mediated emulsion polymerization. For the tPAN NPs, new double peaks related to primary amine group appeared, including peak at 3593 and 3654 cm^{-1}. The peaks related to Schiff base increased, including the Schiff base peak at 1626 cm^{-1} and C=O stretching at 1730 cm^{-1}. [44] On the basis of these data, amidine/Schiff base were successfully introduced on the PAN NPs surfaces.

The optical properties of PAN NPs and tPAN NPs were studied by UV-vis absorption and photoluminescence (PL) spectroscopy. The UV-vis absorption spectrum of the tPAN NPs had absorption enhancement in the UV region (200–300 nm) with a peak at 260 nm compared to that of the PAN NPs (Figure 13). These 260 nm band peak represented a π-π^* transition of the C=N group, which is accordance with FT-IR data. [45] Inset images in Figure 13 illustrated the fluorescence color change from blue (PAN NPs) to bright blue (tPAN NPs)

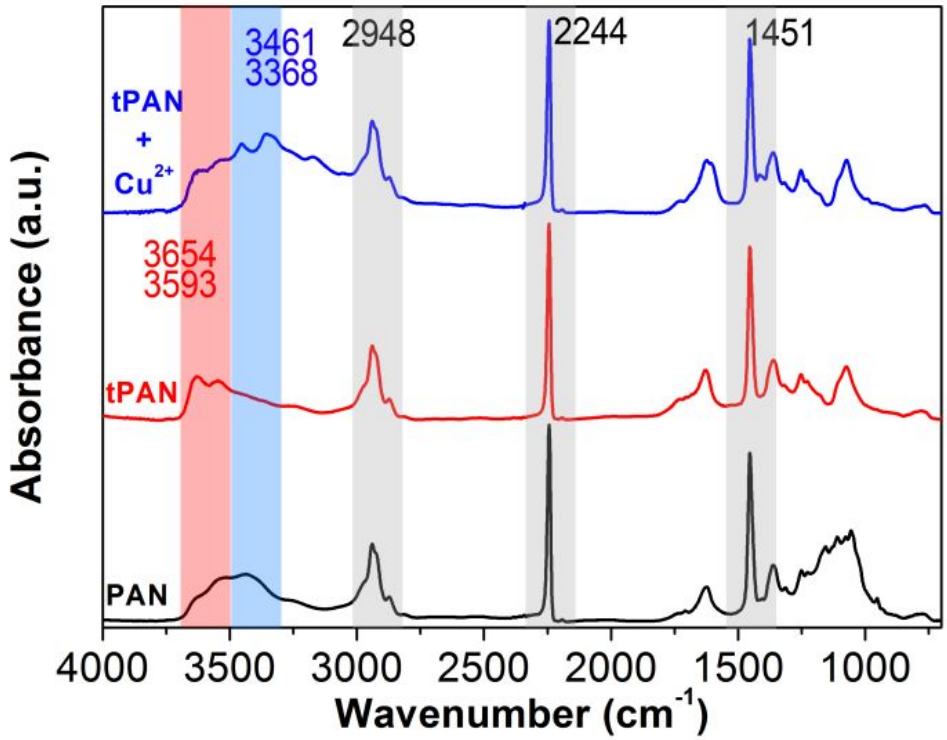

Figure 12. FT-IR spectra of PAN NPs (black), tPAN NPs (red) and tPAN NPs + Cu^{2+} (blue).

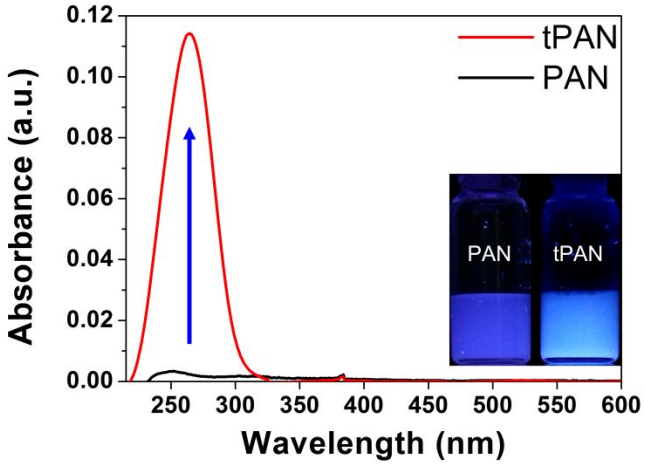

Figure 13. UV-vis absorption spectra of PAN NP and tPAN NPs. The inset shows the photograph of PAN NPs and tPAN NPs under UV light (365 nm).

by surface modification. The fluorescence intensity of the tPAN NPs is 11 times higher than that of the PAN NPs (Figure 14a). Their fluorescence quantum yield was calculated as ca. 0.19 using the standard reference 7-amino-4-methylcoumarin, which is also higher than that of the PAN NPs. [44-46] The increased fluorescence of the tPAN NPs is caused by Schiff base on the surface of the tPAN NPs, which is consistent with other precedent researches (Figure 15). [47,48] We further analyzed excitation dependent emission of the tPAN NPs by changing excitation wavelength from 260 to 320 nm (Figure 14b). The maximum emission intensity of the tPAN NPs was achieved at 410 nm (λex=290 nm), which is optimal excitation wavelength for the experiments. Considering these data, tPAN NPs can be used as intracellular fluorescence sensing probe due to enhanced PL properties.

In order to identify the capability of the tPAN NPs as sensor for copper ion, the selectivity of the tPAN NPs was evaluated by screening various metal ions at a concentration of 10 μM (Figure 16a). The fluorescence of the tPAN NPs was only quenched by addition of copper ions (26% quenching upon addition of 10 μM Cu^{2+}), while no significant quenching effect was observed in other metal ions (Ag^{+}, Al^{3+}, Ca^{2+}, Cd^{2+}, Co^{2+}, Fe^{2+}, Fe^{3+}, Hg^{2+}, K^{+}, Mg^{2+}, Mn^{2+}, Na^{+}, Ni^{+}, Pb^{2+}, and Zn^{2+}). In general, copper ions have a tendency to be coordinated with amidine group due to unshared electron of the nitrogen atoms on the

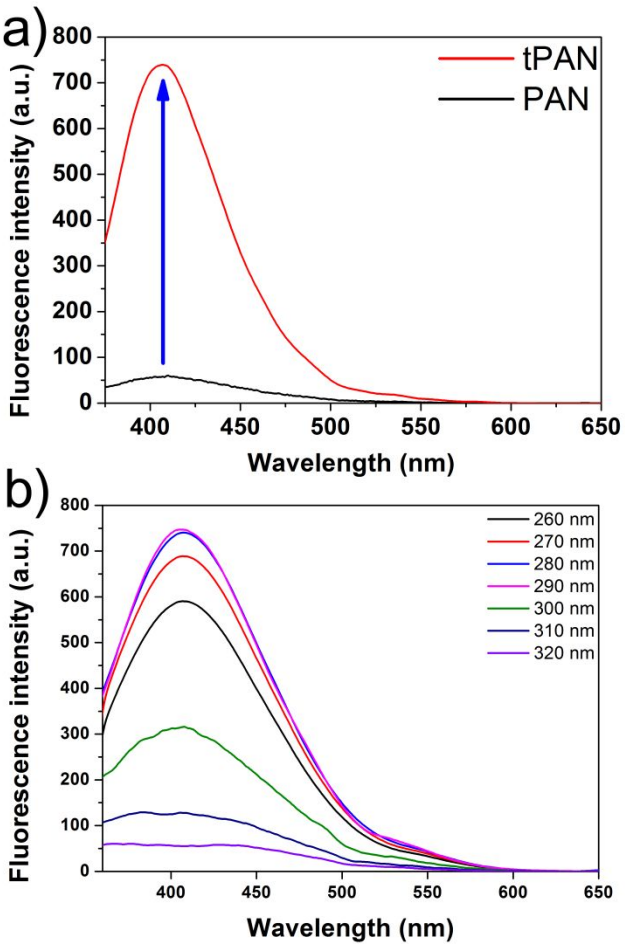

Figure 14. (a) Fluorescence spectra of PAN NP and tPAN NPs. (b) Fluorescence spectra of tPAN NPs under different excitation wavelength.

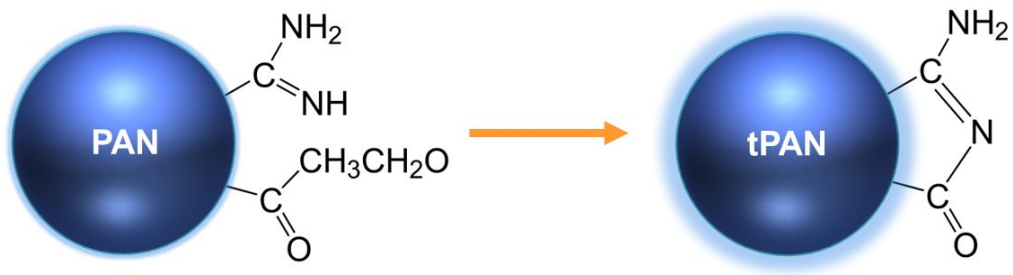

Figure 15. The side reaction in the surface modification for the amidine group. When cyano-groups of PAN react with water, it changes to ester group. Then amidine group reacts with ester group on the tPAN NPs surface, turning into Schiff base which contributes to enhanced fluorescence. Therefore, diverse functional groups including amidine and Schiff bases.

amidine group. [49] Because of its paramagnetic property and unfilled d shell, only copper ion could strongly quench the fluorescence of the tPAN NPs through electron transfer processes. [50-54] To determine the interference effect of tPAN NPs coexisting other metal ions in copper ions detection, the effect of other metal ions on the fluorescence intensity were investigated (Figure 16) and we found that the emission intensity of the tPAN NPs to copper ions was almost unchanged in the presence of other metal ions. The interaction between tPAN NPs and copper ions was confirmed by FT-IR analysis. Figure 15 revealed that the peaks of tPAN NPs at 3593 and 3654 cm^{-1} were shifted to 3368 and 3461 cm^{-1} after copper ion treatment. These changes meant free copper ions were bound with the primary amine groups on the surface of the tPAN NPs. C≡N bond at the 2244 cm^{-1} was not changed, implying the nitrile group on the tPAN NPs was not included in the detection of copper ions. However, as shown in Figure 17, there are no peak shifts of tPAN NPs after addition of some metal ions (Fe^{2+}, Fe^{3+}, Hg^{2+}, and Zn^{2+}), which indicate that copper ions have higher binding affinity with amidine group on the surface of tPAN NPs than other metal ions. The interaction between tPAN NPs and metal ions was also studied by UV–vis absorption (Figure 18). The binding ability of tPAN NPs with various metal ions (Ag^{+}, Al^{3+}, Ca^{2+}, Cd^{2+}, Co^{2+}, Fe^{2+}, Fe^{3+}, Hg^{2+}, K^{+}, Mg^{2+}, Mn^{2+}, Na^{+}, Ni^{+}, Pb^{2+}, and Zn^{2+}) showed

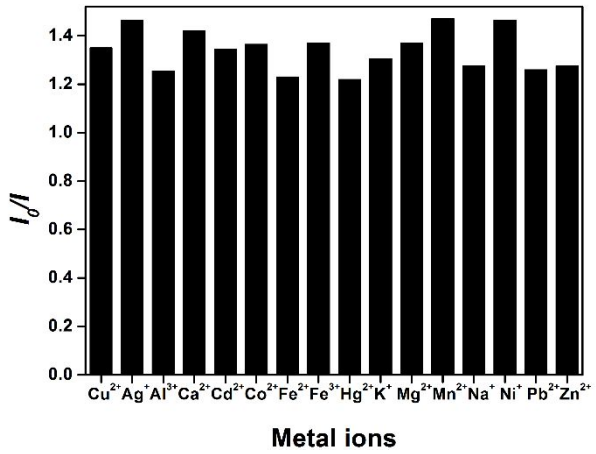

Figure 16. The interference effect of different metal ions (10 μM) on tPAN NPs for Cu^{2+} detection.

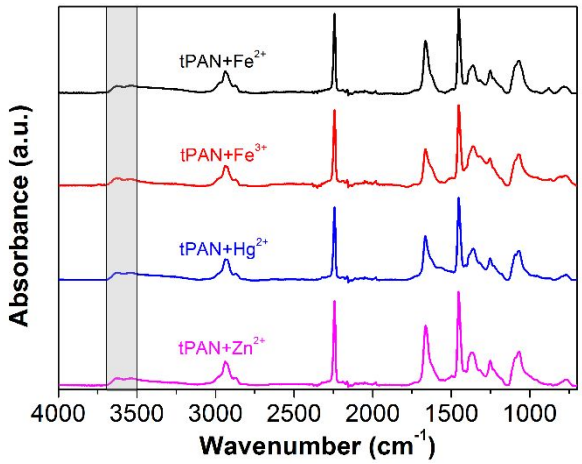

Figure 17. FT-IR spectra of tPAN NPs+Fe^{2+} (black), tPAN NPs+Fe^{3+} (red), tPAN NPs+Hg^{2+} (blue) and tPAN NPs + Zn^{2+} (violet).

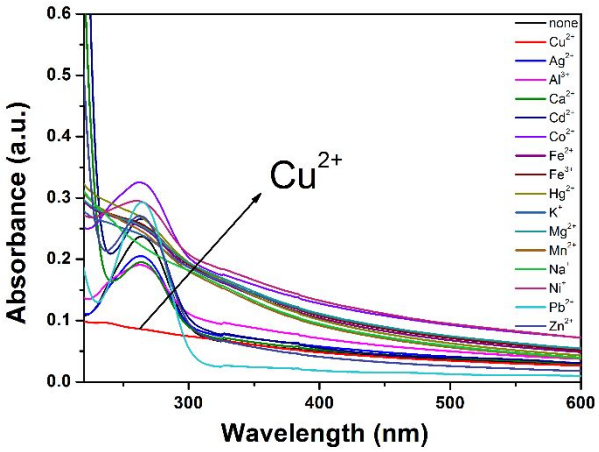

Figure 18. UV–vis absorption spectra of tPAN NPs (10 μg mL^{-1}) upon addition of various metal ions (10 μM) in aqueous solution. Addition of Cu^{2+} resulted in a significant change indicating that the tPAN NPs have higher binding affinity toward Cu^{2+} than other metal ions.

selective response toward Cu^{2+} ions. As shown in Figure 21, addition of Cu^{2+} resulted in a significant change indicating that the tPAN NPs have higher binding affinity toward Cu^{2+} than other metal ions. All these results demonstrate that the tPAN NPs are highly selective for copper ion detection. Based on these analyses, possible interaction between tPAN NPs and copper ions was depicted in the inset images in Figure 19a. As displayed in Figure 5b, fluorescence intensity of the tPAN NPs (10 μg mL-1) decreased by adding copper ions and the peak was blue-shifted from 410 to 370 nm (λex=290 nm). Based on the Figure 19b, fluorescence intensity change of the tPAN NPs was calculated versus copper ion concentration (Figure 19c). The fluorescence intensity remarkably decreased with increasing copper ion concentration. The inset graph showed a linear correlation between the emission intensities and the concentration of copper ions (0-100 nM; adjusted R^2 = 0.991). The limit of detection was 10 nM (3σ of the reagent blank signal), which is 2–3 orders of magnitude lower than previous reports. [43] Additionally, in the physiological concentrations, the minimum concentration of intracellular copper ion is 10 μM, suggesting that the tPAN NPs are suitable as sensitive detection probe for copper ions under the physiological conditions. [43] As a control experiment, ethylenediaminetetraacetate (EDTA) was inserted into the solution containing copper ion and tPAN NPs (Figure 19d). EDTA can chelate with metal ions in a

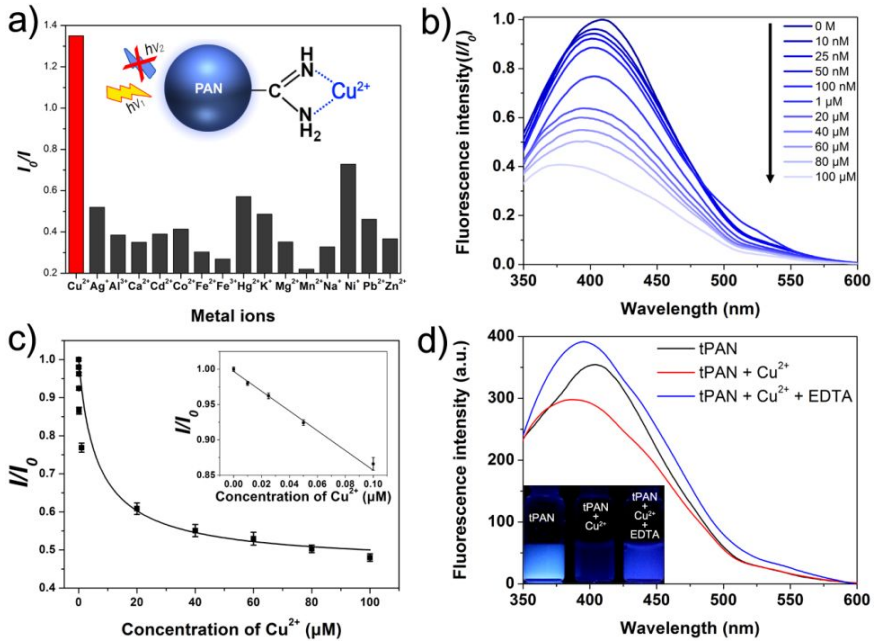

Figure 19. (a) Selectivity of tPAN NPs (10 μg mL^{-1}) for different metal ions (10 μM). Inset represents the possible sensing mechanism of tPAN NP for Cu^{2+}. (b) Fluorescence emission spectra of tPAN NPs in the presence of Cu^{2+} at different concentrations (0-100 μM). (c) Based on the Figure 5b, the relationship between emission fluorescence intensity of tPAN NPs and concentrations of Cu^{2+} was calculated. I and I_0 are the emission fluorescence intensities of the tPAN NPs at 410 nm (λ_{ex}=290 nm) in the presence and absence of Cu^{2+}, respectively. Inset is the linear region. (d) Representative fluorescence spectra with the addition of Cu^{2+} and EDTA in the quenching recovering. The inset shows the fluorescence photograph of tPAN NPs, tPAN NPs + Cu^{2+}, and tPAN NPs + Cu^{2+} + EDTA under UV light (365 nm).

1:1 ratio, which induces removal of the metal ions from the solution. [53] The quenched fluorescence of the tPAN NPs in the presence of copper ion was ecovered into strong fluorescence by EDTA treatment (inset images in Figure 19d). Taking these facts into account, tPAN NPs are proper sensors for copper ion detection with high sensitivity and selectivity against other metal ions.

3.1.2. Application for Intracellular Copper Ion Detection

The sensing ability of the tPAN NPs was systematically investigated in vitro. SK-BR-3 cells were incubated with 10 μg mL^{-1} tPAN NPs for 24 h (Figure 20a). Amidine group of the tPAN NPs possess positive surface charge, leading to adhesion between tPAN NPs and the plasma membrane of the cells.32 Internalized tPAN NPs exhibited blue fluorescence in the cytoplasm, making tPAN NPs possible to detect copper ions in cells. Then, the copper ions were inserted into the culture medium for 20 min, and the blue fluorescence of the tPAN NPs was turned off in the presence of copper ions (Figure 20b). Upon addition of same concentration of copper ions (Figure 21), the intensity of blue emission from the tPAN NPs distinctively decreased, which agreed well with a change of the blue fluorescence observed in SK-BR-3 cells. Then, excess EDTA was added to copper ion containing culture medium to eliminate copper ions. The strong fluorescence of tPAN NPs re-appears as shown in Figure 20c. These data implie that tPAN NPs is easily introduced into cells and can be used as a fluorescence sensor for copper ions in living cells.

For using tPAN NPs as intracellular sensor probe, low cytotoxicity of the tPAN NPs is required. Cytotoxicity of the tPAN NPs was determined by two methods (Figure 22); adenosine triphosphate (ATP) based viability test and generation of ROS by tPAN NP treatment. First, ATP concentrations of tPAN

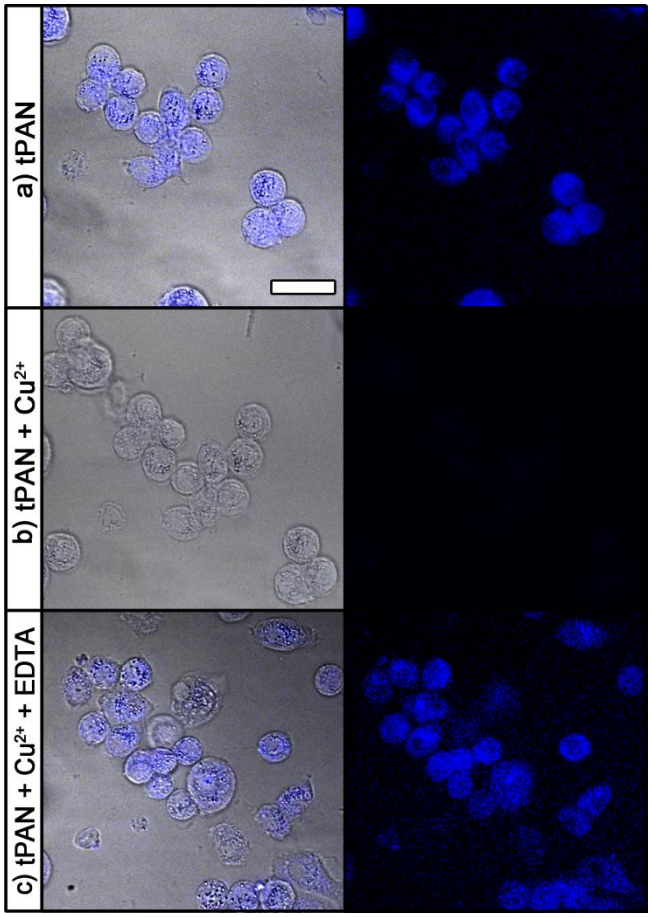

Figure 20. Live cell differential interference images of tPAN NPs-treated SK-BR-3 cells; (a) images are before treatment of Cu^{2+}, (b) images are 20 min after treatment of 10 μg/mL Cu^{2+} and (c) images are 20 min after treatment of 100 μg/mL EDTA. Scale bars = 50 μm.

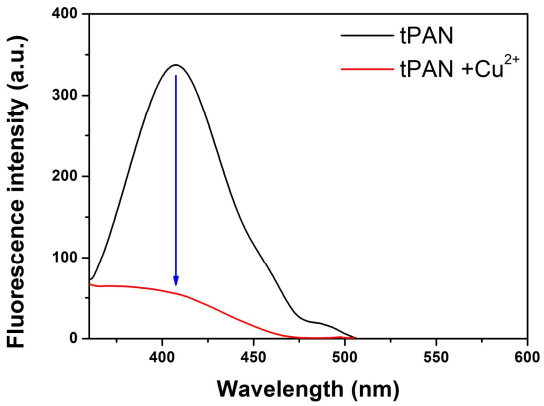

Figure 21. Fluorescence emission spectra of tPAN NPs with the addition of Cu^{2+} (10 μg mL^{-1}).

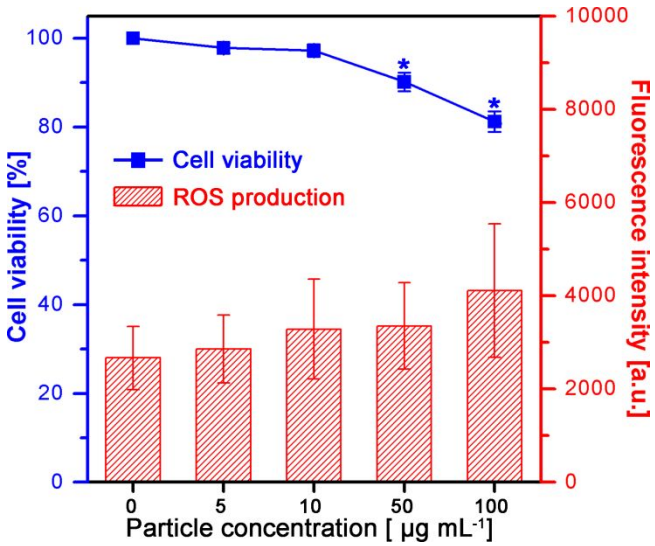

Figure 22. Viability of SK-BR-3 cells incubated with tPAN nanoparticles for 24 h. The viability was calculated relative to a negative control. ROS production by SK-BR-3 cells after being incubated with tPAN. H_2O_2 (0.02%) was used as a positive control. Values exhibit mean ± SD, and each experiment was performed in triplicate.

NP treated SK-BR-3 cells were measured by transformation of luciferin to oxyluciferin. Until a concentration of 10 μg mL^{-1}, tPAN NPs have no significant effect on the cell viability. The viability was over 80% even at a high concentration of the tPAN NPs (100 μg mL^{-1}) for 24 h incubation. We also evaluate production of ROS in tPAN NP-added SK-BR-3 cells by 2',7'-dichlorodihydrofluorescein diacetate (H2DCF-DA) staining. After tPAN NP treatment, compared to negative control, ROS production increased within the margin of error. Collectively, tPAN NPs can be applied as intracellular copper ion detector without significant viability decrease or ROS production. Therefore, tPAN NPs offers a selective detection probe for copper ion in living cells with low toxicity.

3.2. Au-decorated PAN Nanoparticles with Dual-Emission and Their Application

3.2.1. Fabrication of Au-decorated PAN Nanoparticles with Dual-Emission

Figure 23 illustrated a schematic diagram of the fabrication of the Au-PAN NPs used in this study. PAN NPs were fabricated by ultrasonic mediated emulsion polymerization, as previously reported in part 3.1.1. [40] The gold nanoclusters (AuNCs) were fabricated by reduvtion of $HAuCl_4$ with L-fglutathione (GSH). According to the prvious report, GSH aqueous solution (6 mM, 10 mL) was mixed with $HAuCl_4$ aqueous solution (4 mM, 10 mL) under srtirred condition at 90 for 6.5 h. The as-synthesized AuNCs decorated tPAN NPs (Au-PAN NPs) emit dual fluorescence; orange and blue fluorescence were respectively from the AuNCs and tPAN NPs. The AuNCs have capability to detect Hg(II) ion selectively, the surface of the gold nanoparticle was modified with mercaptopropionic acid (MPA) and homocystine (bound to the gold nanoparticle surface through a Au-S bond). The gold nanoparticle surface was attached with MPA and Hcy through a -SH bond. As a result of Hg(II) detection the fluorescence of Au-PAN NPs was changed from violet to blue. Therefore, the fluorescence intensity ratio between tPAN NPs and AuNCs by addition of mercury ions provides the information of selective detection for

Hg(II).

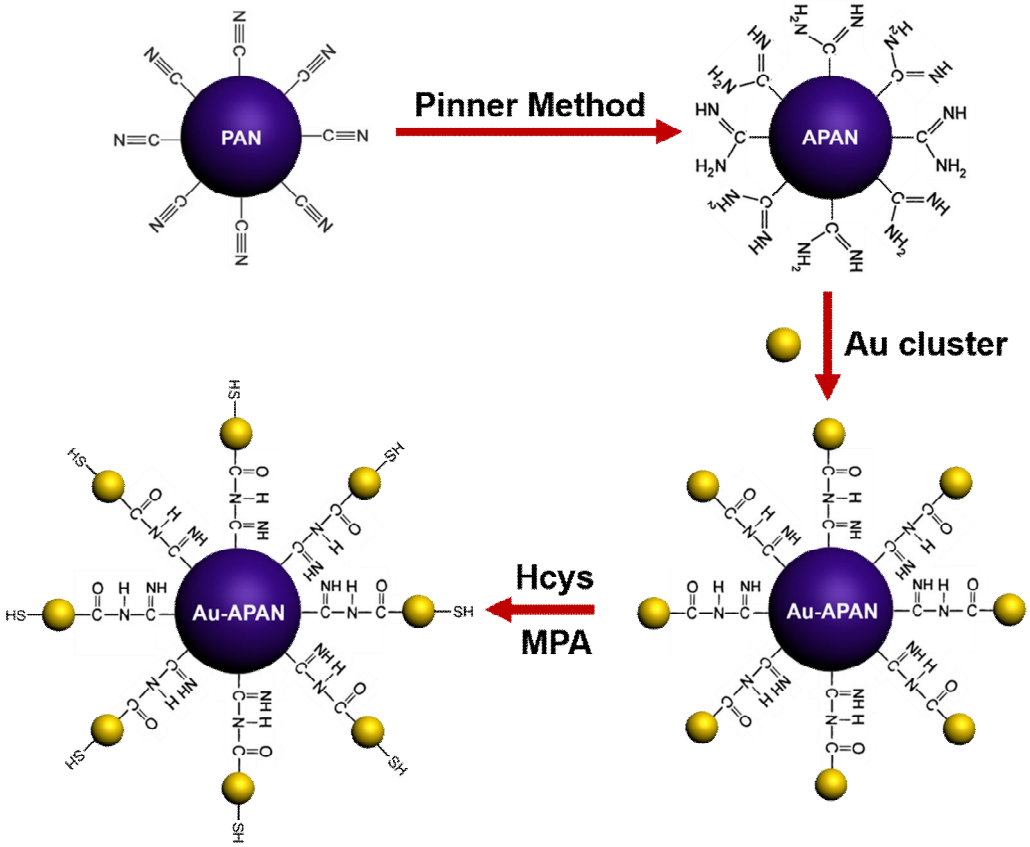

Figure 23. Schematic diagram of fabrication of tPAN NPs and Au-PAN NPs.

In Figure 24a and b, AuNCs and tPAN NPs were uniform sphere in shape with diameter of ca.2nm and 51 nm, respectively. After decoration of AuNCs on the surface of the tPAN NPs, the dark spots in Figure 24c denoted the successful incorporation of AuNCs on the tPAN NPs. The amount of decorated AuNCs on the tPAN NPs was measured as *ca.* 24.3 wt% by inductively coupled plasma emission spectrometer (ICP) analysis.

Formation of the PAN NPs, tPAN NPs and the Au-PAN NPs was confirmed by Fourier-transform infrared (FT-IR) spectrometry (Figure 25). FT-IR spectrum of the PAN NPs showed characteristic PAN peaks, including the C≡N stretching bands at 2244 cm^{-1}, the C-H stretching peak at 2948 cm^{-1}, and C-H deformation peak at 1451 cm^{-1}. These peaks revealed successful polymerization of the PAN NPs by ultrasonic mediated emulsion polymerization. For the tPAN NPs, new double peaks related to primary amine group appeared, including peak at 3593 and 3654 cm^{-1}. The peaks related to Schiff base increased, including the Schiff base peak at 1626 cm^{-1} and C=O stretching at 1730 cm^{-1}. [44] After AuNCs conjugation on the tPAN NPs, new two peaks were appeared; N-H deformation peak at 1554 cm^{-1}, secondary amine stretching peak at 3335 cm^{-1}. The presence of AuNCs was futher confirmed by XPS spectra and enlarged Au 4f spectra (Figure 25b and c). On

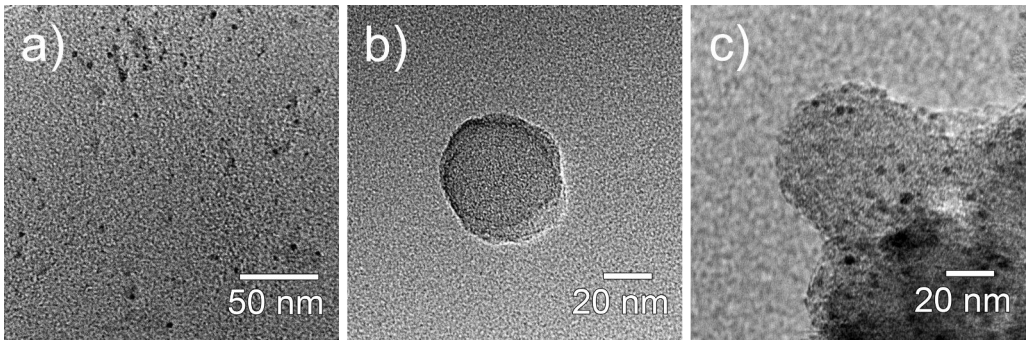

Figure 24. TEM images (a) AuNCs, (b) PAN NPs and (c) Au-PAN NPs. AuNCs and tPAN NPs were uniform sphere in shape After decoration of AuNCs on the surface of the tPAN NPs, the dark spots.

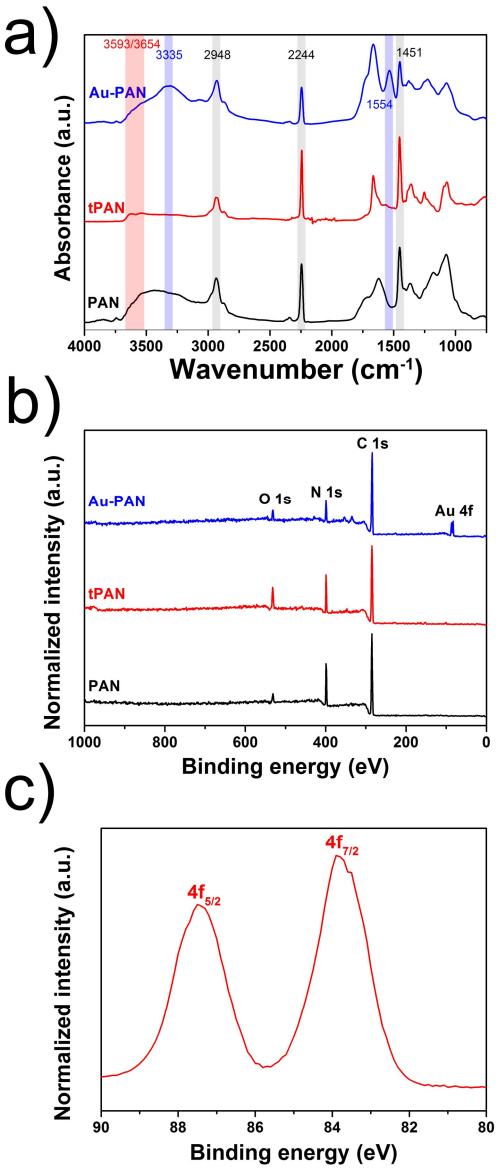

Figure 25. (a) FTIR spectra of PAN (black), tPAN (red), and Au-PAN NPs (blue). (b) XPS spectra of PAN (black), tPAN (red), and Au-PAN NPs (blue). (c) Enlarged Au 4f spectrum of Au-PAN NPs.

the basis of these data, amidine group and AuNCs were successfully introduced on the PAN NPs surfaces.

Figure 26 displays representative absorbance and fluorescence spectra of AuNCs, tPAN NPs and Au-PAN NPs. The UV-vis absorption spectrum of the tPAN NPs had absorption enhancement in the UV region (200–300 nm) with a peak at 260 nm compared to that of the PAN NPs (Figure 26a). These 260 nm band peak represented a π-π* transition of the C=N group, which is accordance with FT-IR data. [45] The AuNCs was showed a broad absorption band and emitted a strong orange fluorescenc at 570 nm (λ_{ex}=350 nm) due to quantum confinement effect, which is similar result to previous reports. [44] Inset images in Figure 26a illustrated the fluorescence color change from blue (PAN NPs) and orange (AuNCs) to violet (Au-PAN NPs) by surface introduction. Although the absorbance spectrum of Au-PAN NPs was more similar to that of AuNCs than tPAN NPs, Au-PAN NPs exhibited a dual-emission spectrum with two distinct fluorescence peaks (λ_{ex}=340 nm); one is at 420 nm from the tPAN NPs, and the other is at 570 nm from the decorated AuNCs on the surface of the tPAN NPs, which were separted by 150 nm (Figure 29b). We further analyzed excitation dependent emission of the Au-PAN NPs by changing excitation wavelength from 300 to 360 nm (Figure 26c). As excitation wavelength was increased from 300 to 360 nm, the emitted fluorescence

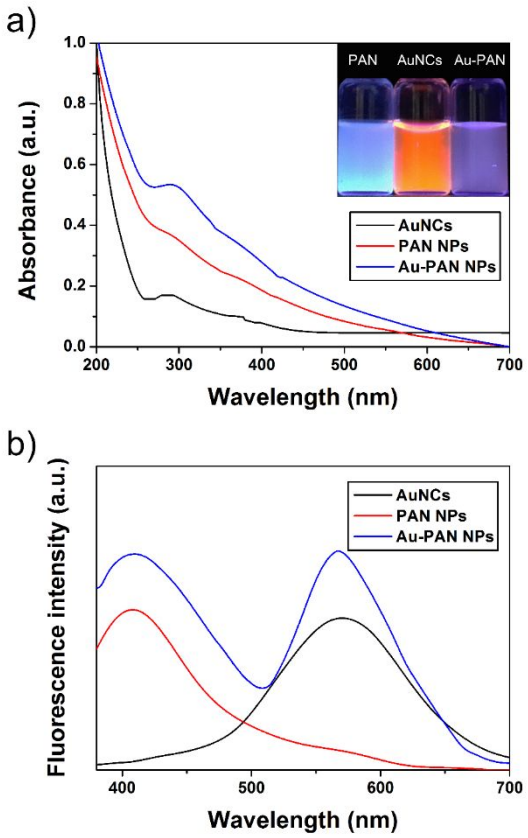

Figure 26. (a)UV-vis absorprion spectra and (b) the representative fluorescence spectra of the AuNCs (black), tPAN (red), and Au-PAN NPs (blue).

intensity of tPAN NPS was gradually increased, while that of AuNCs decreased simultaneously. The equal emission intensity of the Au-PAN NPs was achieved at 340 nm excitation, which is optimal excitation wavelength for the experiments. Considering these data, Au-PAN NPs can be used as fluorescence sensing probe due to enhanced PL properties. Their fluorescence quantum yield was calculated as *ca.* 0.19 (tPAN NPs) and *ca.* 0.11 (AuNCs) using the standard reference 7-amino-4-methylcoumarin, respectively.

3.2.2. Application for Mercury Ion Detection

The energy transfer between PAN NPs and AuNCs (quencher) is the main reason of strong fluorescence quenching. [55,56]. The Au-PAN NPs were used as a PL responsive probe for metal ion sensing. Figure 27 represents the PL response of the nanocomposite with addition of different metal ions. A significant intensity ratio of the two emission wavelengths (I_{420}/I_{570}) increasing is observed in presence of Hg^{2+} (Figure 30). Interestingly, other metal ions; alkaline earth (Li^{+}, Na^{+}, K^{+}, Mg^{2+}, Ca^{2+}) and transition heavy metal ions (Pb^{2+}, Pb^{+}, Mn^{2+}, Fe^{2+}, Cu^{2+}, Ni^{2+}, Zn^{2+}, Cd^{2+}) do not have a momentous effect on PL signal of Au-PAN NPs. Only 43% increasing intensity ratio (I_{425}/I_{570}) of the Au-PAN NPs is observed for Hg^{2+} ion, which is much smaller than the change of intensity ratio by Hg^{2+}. Figure 27 inset image shows the colorimetric response under UV light. The high selectivity of toward mercury ion can also be observed by the naked eye, and only mercury ion induces an obvious color change under visible or UV light. To determine the interference effect of Au-PAN NPs coexisting other metal ions in mercury ions detection, the effect of other metal ions on the fluorescence intensity were investigated (Figure 28) and we found that the emission intensity of the Au-PAN NPs to mercury ions was almost unchanged in the presence of other metal ions. In a mixture, in which all salts are present, that is, Li^{+}, Na^{+}, K^{+}, Mg^{2+}, Ca^{2+}, Pb^{2+}, Pb^{+}, Mn^{2+},

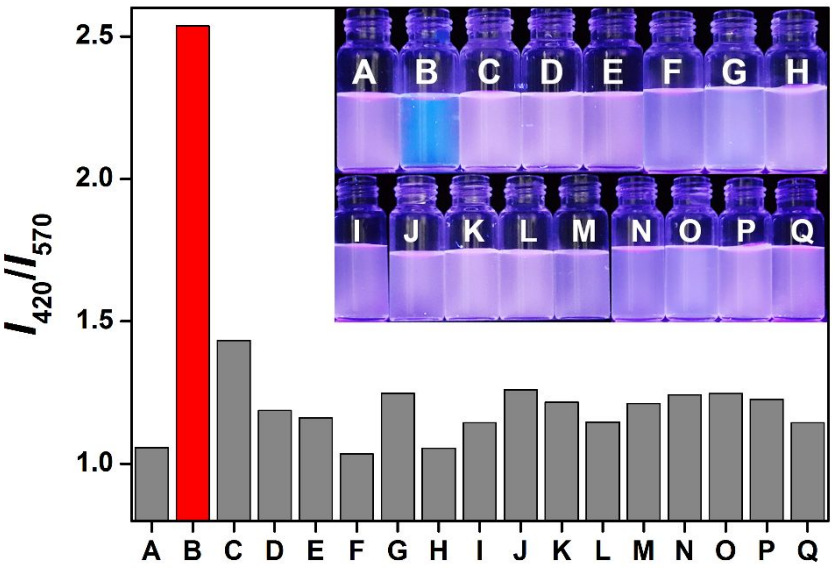

Figure 27. The emission ratio (I_{420}/I_{570}) of Au-PAN NPs (50 μg mL^{-1}) in the presence of various analytes (10 μM) in PBS for 60 min. A) blank; B) Hg^{2+}; C) Cu^{2+}; D) Al^{3+}; E) Ni^{2+}; F) Cr^{2+}; G) Co^{2+}; H) Pb^{2+}; I) Fe^{2+}; J) Mg^{2+}; K) Zn^{2+}; L) Cd^{2+}; M) Sr^{2+}; N) Ca^{2+}; O) Fe^{3+}; P) K^{+}; Q) Li^{2+}

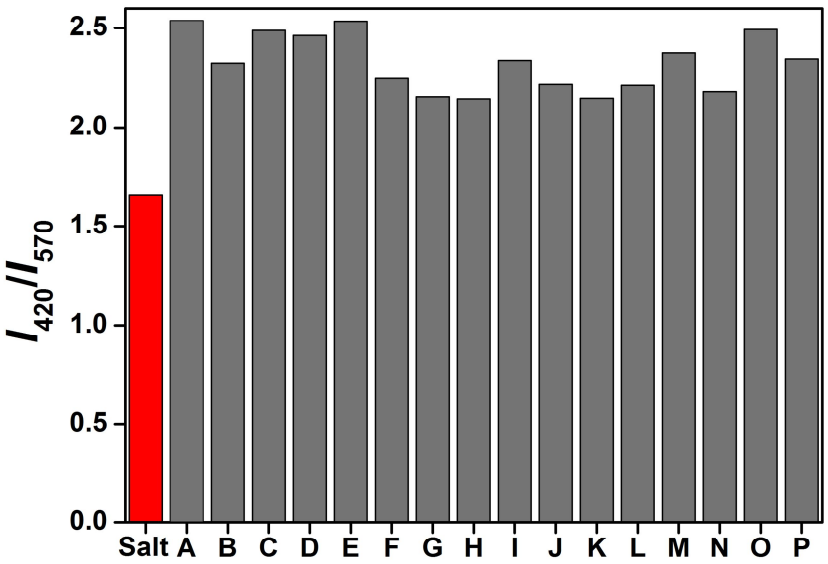

Figure 28. The interference effect of different metal ions (10 μM) on tPAN NPs for Hg^{2+} detection.

Fe^{2+}, Co^{2+}, Ni^{2+}, Zn^{2+}, Cd^{2+} and Cu^{2+} (except Hg^{2+}), 60% increasing intensity ratio (I_{425}/I_{570}) of the Au-PAN NPs probe is observed. As 43% PL quenching is caused by Cu^{2+}, thus 60% increasing intensity ratio (I_{425}/I_{570}) in the mixture is mainly due to the presence of Cu^{2+} only. It reveals that Au-PAN NPs nanocomposite is almost insensitive to the other salts. The histograms of increasing intensity ratio (I_{420}/I_{570}) by individual metal ions as well as in mixture are shown in the Figure 28 reveals the very high selectivity of this nanocomposite probe to Hg^{2+}. As displayed in Figure 29a, fluorescence intensity of the Au-PAN NPs (10 μg mL^{-1}) changed by adding mercury ions. The added mercury ions have effect on both two emission wavelengths of Au-PAN NPs; a peak intensity at 420 nm rapidly increased, whereas a peak at 570 nm showed gradual decline. The ratios of fluorescence intensities at 420 nm and 570 nm showed a linear relationship (Figure 29b) with increasing mercury ion concentrations, suggesting that the Au-PAN NPs can be used as ratiometric sensor for Hg^{2+}. From the slope of the linear plot, we have calculated the limit of detection of Hg^{2+} concentration to be 1 nM, which is within the range set by USEPA. Noteworthy, the maximum allowed concentration of Hg^{2+} is 10 nM in drinking water according to USEPA. [57,58] The sensing behavior of Au-PAN NPs was examined with UV−vis absorption spectroscopy. Upon introducing increasing concentrations of Hg^{2+} (0−200 nM) to the solution of Au-PAN NPs

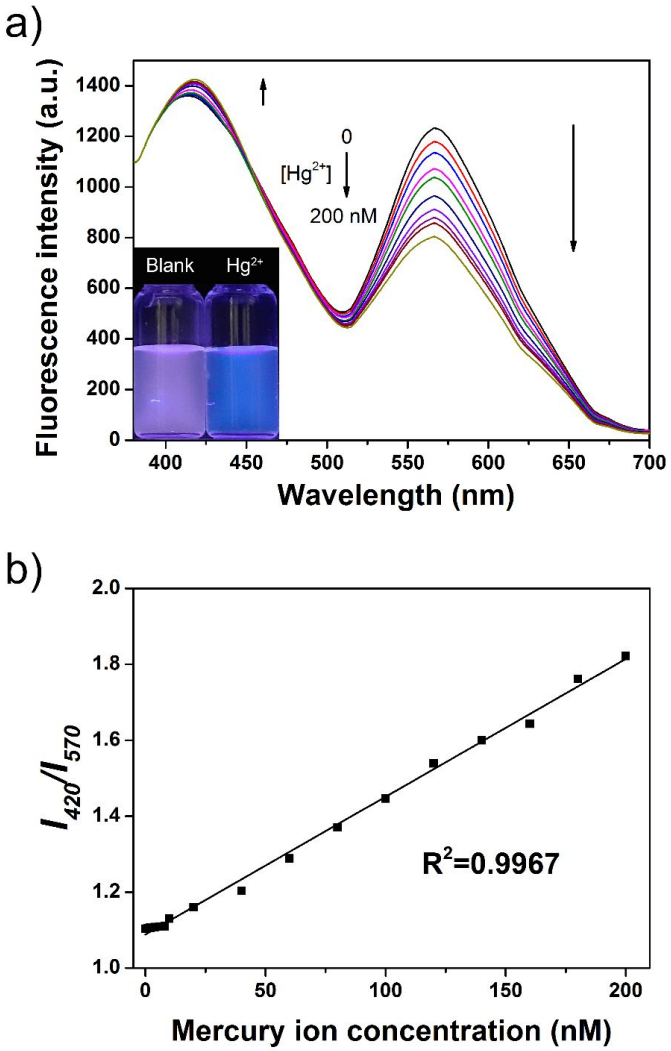

Figure 29. (a) Fluorescence emission spectra of Au-PAN NPs in the presence of Hg^{2+} at different concentrations (0-200 nM). (b) Based on the Figure 32a, the relationship between emission fluorescence intensity of Au-PAN NPs and concentrations of Hg^{2+} was calculated.

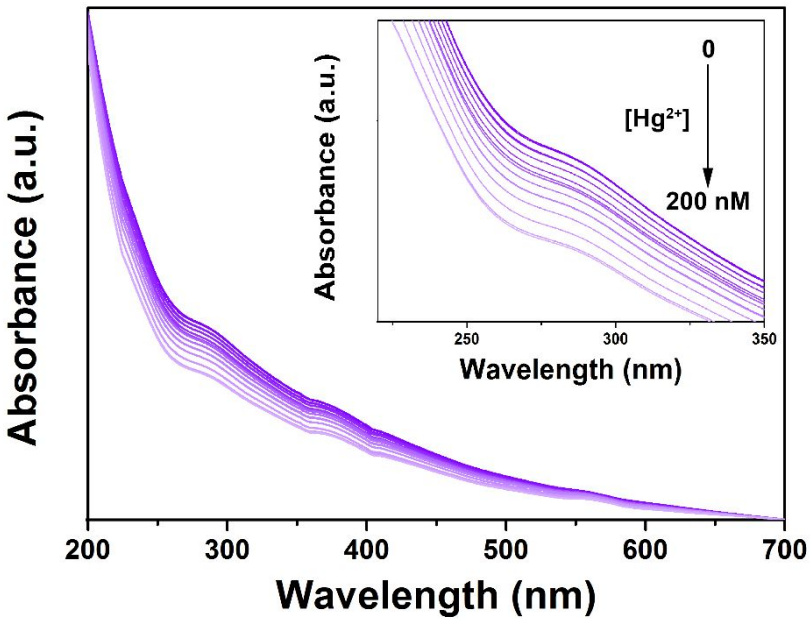

Figure 30. Uv-vis spectra of Au-PAN NPs in the presence of Hg^{2+} at different concentrations (0-200 nM).

in distilled water at room temperature (25 °C). The absorption peak of Au-PAN NPs at 280 nm gradually decreases with the increasing concentrations of Hg^{2+} (Figure 30).

3.3. Au-decorated Graphene Quantum Dots with Dual-Emission and Their Application

3.3.1. Fabrication of Au-decorated Graphene Quantum Dots with Dual-Emission

Figure 31 illustrates the schematic process of fluorescent Au-GQD sensor and selective sensing of Cys into the target cancer cell. Initially, pristine blue photoluminescent GQDs (P-GQDs) were fabricated *via* an excessive oxidation and size-selective precipitation procedure as described in previously described. [59] To graft the sensing moiety of Cys onto the P-GQDs, AuNCs was bonded onto the P-GQDs *via* NHS/EDC reaction (Au-GQDs). The as-synthesized Au-GQDs were internalized in the MCF-7 cell (folate receptor overexpressed cells) *via* the FA-mediated targeting. Reaction with intracellular Cys made Au-S of the Au-GQD into AuNCs, which induced efficient electronic communication between the Au-GQDs and Cys. [60] By the reaction with EDC, a carboxylic acid group on the surface of P-GQDs was converted to an active intermediate which reacts with NHS to give relatively stable amine-reactive NHS-ester. [61] Then, the amine group of folic acid (FA) nucleophilically attacked the NHS-ester to form an amide bond, leading to covalent linkage to Au-GQDs (FA-Au-GQDs). Among various targeting system, the FA was selected as model targeting agent for enhancing internalization and selectivity of cancer cells.

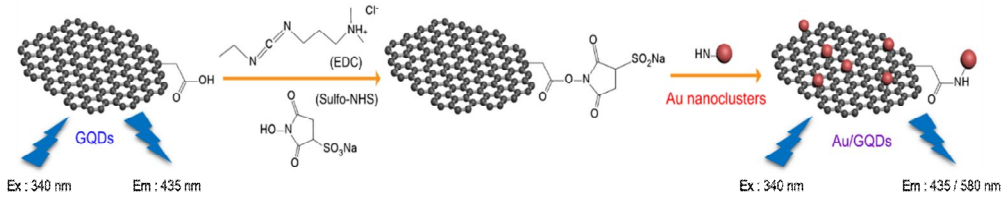

Figure 31. Schematic diagram of fabrication of FA-Au-GQDs

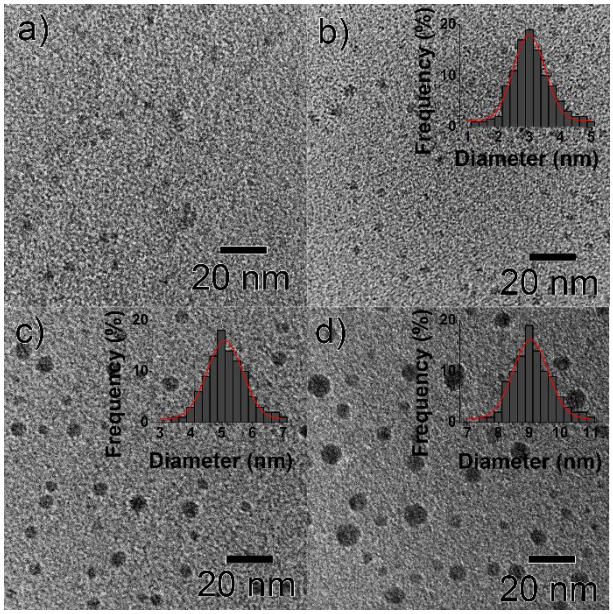

Figure 32. TEM images (a) AuNCs, (b) GQDs (c) Au-GQDs and (d) FA-Au-GQDs

According to the target cell type, the FA can be easily substituted by other antibody. To the best of our knowledge, this is the first attempt to apply GQD as photoinduced electron transfer (PET) based sensor probes for intracellular cysteine.

To confirm the formation of GQDs (P-GQD, Au-GQD and FA-Au-GQD), high-resolution transmission electron microscopy (HR-TEM) analysis and size-distribution analysis was conducted. As displayed in Figure 32, the AuNCs and the P-GQDs were uniform and monodispersed with average diameter of ~3 nm. After the functionalization of P-GQD with AuNCs, the Au-GQD exhibited higher atomic density compared to P-GQD, and the average diameter increased to ~4.8 nm (figure 2b). Following treating folic acid onto the Au-GQD, FA-Au-GQD exhibited average diameter further increased to ~8.8 nm, indicating successful functionalization of FA-Au-GQD (Figure 32). The formation of GQDs was confirmed using both fourier-transform infrared (FT-IR) spectroscopy and X-ray photoelectron spectroscopy (XPS). In figure 33, the FT-IR spectrum of the P-GQD shows characteristic C–H deformation peaks at 835 cm^{-1}, C–O–C stretching peaks 1236 cm^{-1}, C–O stretching peaks at 1360 cm^{-1}, and C=C aromatic stretching peaks at 1591 cm^{-1}, indicating the successful synthesis of P-GQD. In case of Au-GQD, the peaks related to amines increased in intensity, including the N–H bending mode at 655 cm^{-1}

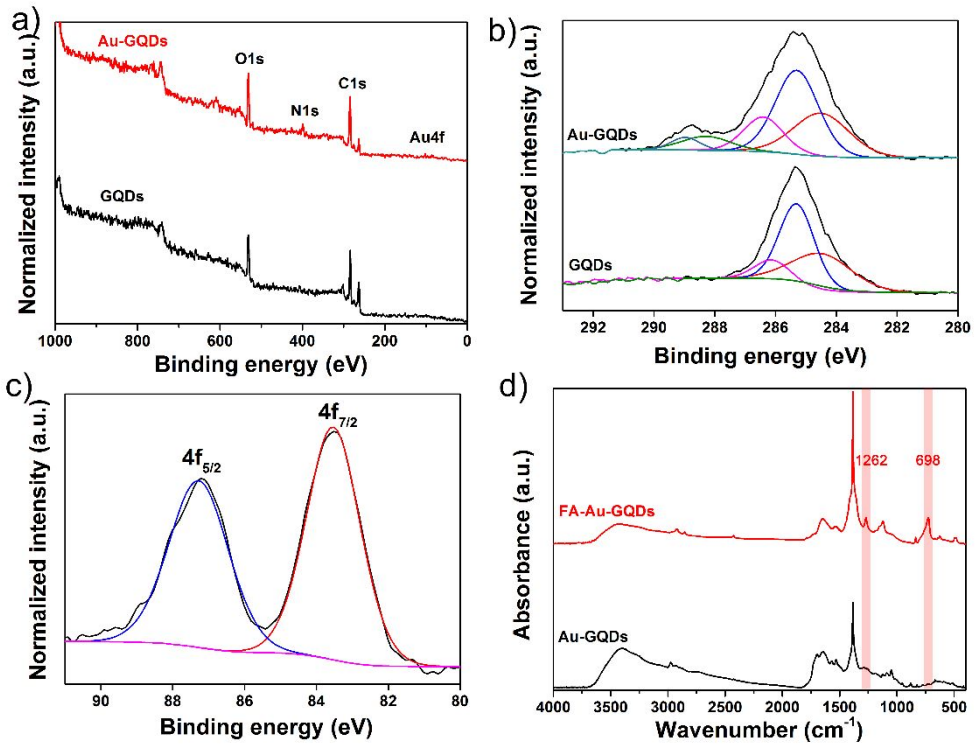

Figure 33. (a) XPS spectra of GQDs (black) and Au-GQDs (red) (b) Enlarged C 1s spectrum of GQDs and Au-GQDs (c) Enlarged Au 4f spectrum of Au-GQDs . (a) FT-IR spectra of Au-GQDs (black) and FA-Au-GQDs (red).

and 1530 cm^{-1} and C–N stretching modes at 1179 cm^{-1} and C=N stretching at 1690 cm^{-1}. On the basis of these data, FA and AuNCs successfully modified the B-GQD surfaces. Figure 33a shows XPS characterization of P-GQD, including surface-modified Au-GQD and FA-Au-GQD. The atomic concentrations of C, N, and O in the GQDs were determined to be 54.78%, 0.12%, and 45.10%, respectively. In the F-GQD, the atomic concentrations were 48.17% (C), 4.64% (N), and 47.19% (O), which indicates that the N 1s region was enlarged. The deconvoluted C1s XPS spectrums of P-GQD and Au-GQD, are presented in figure 33b. The main peaks of GQD at 284.6 eV (peak I) corresponds to the graphite-like sp^2 carbon, indicating most of the carbon atoms are arranged in honeycomb lattice.[1] In addition, the small peaks of P-GQD can be attributed to C−O (peak II, 286.0 eV), −COOR (peak III, 287.8 eV), and CO_3^{2-} (peak IV, 290.1 eV), respectively. After the AuNCs treatment, the peak intensity related to C−N bonding (peak II and III) significantly increased in Au-GQD, which can be attributed to the functionalization of P-GQD by conjugation with AuNCs. As the above results, XPS spectra and enlarged C1s spectra confirmed the successful fabrication of Au-GQD.

Figure 34 displays representative absorbance spectra of Au-GQD and FA-Au-GQD. UV-Vis spectra showed a new shoulder peak at 265 nm in FA-Au-GQD due to surface modification of Au-GQD with AuNCs though amide bond.

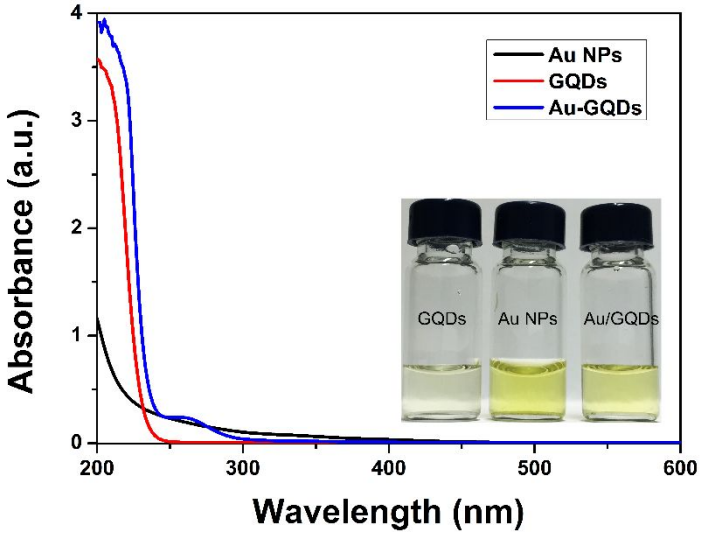

Figure 34. UV absorbance spectra of AuNCs (black line), GQDs (red line), FA-Au-GQDs (blue line).

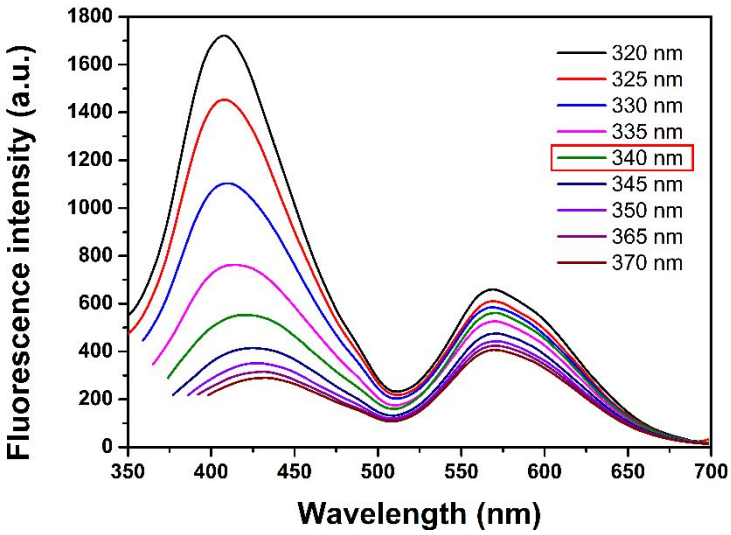

Figure 35. Fluorescence emission spectra of FA-Au-GQDs in the different wavelengths.

Figure 34 shows that Au-GQD had optimal excitation and emission wavelengths at 340 nm and 435/570 nm. The fluorescence quantum yield of the Au-GQD was calculated as *ca.* 0.02 (blue) using the standard reference, 7-amino-4-methylcoumarin. In the previous research, the fluorescence quantum yield of boronate-modified polyacrylonitrile nanoparticles is only *ca.* 0.10. [62] Although the absorbance spectrum of FA-Au-GQDs was more similar to that of AuNCs than GQDs, FA-Au-GQDs exhibited a dual-emission spectrum with two distinct fluorescence peaks (λ_{ex}=340 nm); one is at 435 nm from the GQDs, and the other is at 580 nm from the decorated AuNCs on the surface of the GQDs, which were separted by 155 nm (Figure 35). We further analyzed excitation dependent emission of the FA-Au-GQDs by changing excitation wavelength from 320 to 370 nm (Figure 35). As excitation wavelength was increased from 320 to 370 nm, the emitted fluorescence intensity of FA-Au-GQDs was gradually increased, while that of AuNCs decreased simultaneously. The equal emission intensity of the FA-Au-GQDsN was achieved at 340 nm excitation, which is optimal excitation wavelength for the experiments. Considering these data, FA-Au-GQDs can be used as fluorescence sensing probe due to enhanced PL properties.

To further verify the selectivity, FA-Au-GQDs was incubated with the representative biologically relevant species in PBS buffer (pH 7.4). As shown

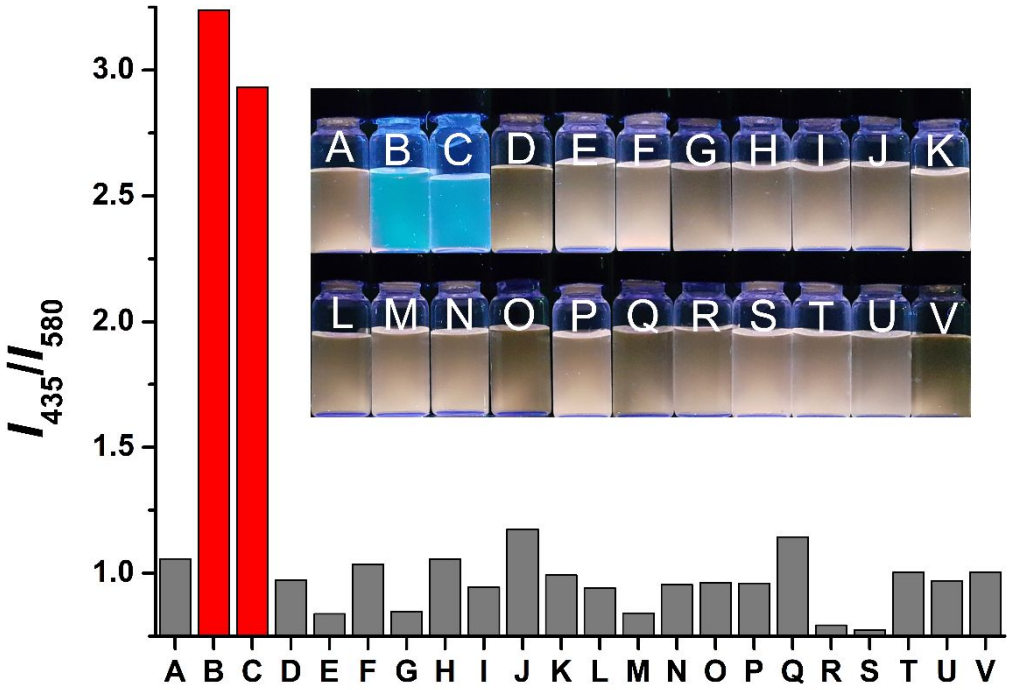

Figure 36. The emission ratio (I_{435}/I_{580}) of FA-Au-GQDs (50 μg mL^{-1}) in the presence of various analytes (1 mM) in PBS for 60 min. A) blank; B) Cys; C) Hcy; D) His; E) Thr; F) Leu; G) Asp; H) Arg; I) Tyr; J) Pro; K) Iso; L) Try; M) Met; N) Val; O) Lys; P) Ala; Q) Gln; R) Gly; T) Glu; U) Ser; V) Phe.

in Figure 36, only Cys/Hcy induces a dramatic increment of the emission ratio, while other amino acids (His, Thr, Leu, Asp, Arg, Tyr, Pro, Iso, Try, Met, Val, Lys, Ala, Gln, Gly, Glu, Ser, Phe). The high selectivity of FA-Au-GQDs toward Cys/Hcy can also be observed by the naked eye, and only Cys/Hcy induces an obvious color change under visible or UV light (Figure 36 inset image). As displayed in Figure 37a, fluorescence intensity of the FA-Au-GQDs (10 μg mL^{-1}) changed by adding Cys/Hcy. The added Cys/Hcy have effect on both two emission wavelengths of FA-Au-GQDs; a peak intensity at 435 nm rapidly increased, whereas a peak at 580 nm showed gradual decline. Figure 37a inset image shows the colorimetric response under UV light. The ratios of fluorescence intensities at 435 nm and 580 nm showed a linear relationship (Figure 37b) with increasing Cys/Hcy concentrations, suggesting that the FA-Au-GQDs can be used as ratiometric sensor for Cys/Hcy. From the slope of the linear plot, we have calculated the limit of detection of Cys/Hcy concentration to be 5 nM. It has been observed that intensity ratio of FA-Au-GQDs increases with detecting time (Figure 38). The saturation of intensity ratio is observed after 40 sec, which indicates the completion of the reaction between FA-Au-GQDs and Cys/Hcy.

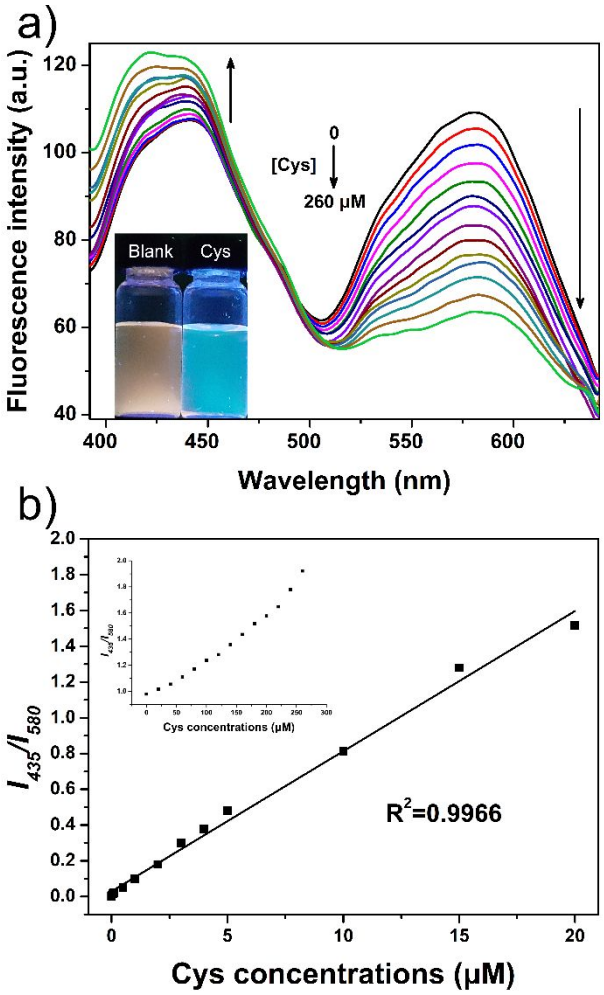

Figure 37. (a) Fluorescence emission spectra of gold cluster decorated GQDs in the presence of Cys at different concentrations. (b) Based on the Figure 39a, the relationship between emission fluorescence intensity of FA-Au-GQDs and concentrations of Cys/Hcy was calculated. Inset is the linear region.

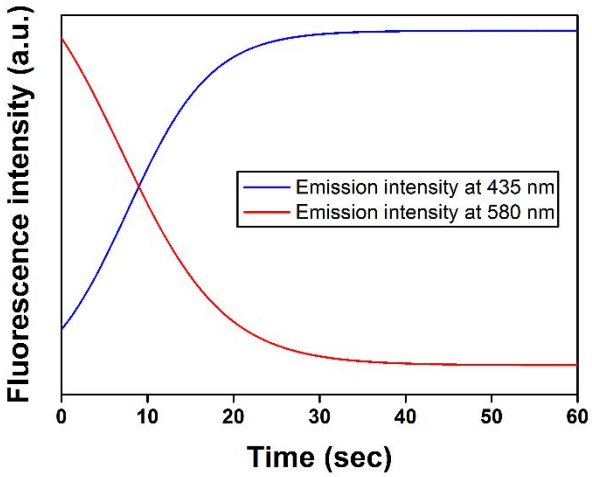

Figure 38. Time-dependent fluorescence intensity plot of FA-Au-GQDs after Cys/Hcy insertion (5 nM; detected at 435 nm emission and 580 nm, respectively)

3.3.2. Application for Intracellular Cysteine Detection

On the basis of these data, the sensing capability of the FA-Au-GQDs was systematically investigated *in vitro*. In our experiments, two cell lines were used: MCF-7 (folate receptor overexpressed cell; target; FR+) and SK-BR-3(absence of folate receptor; control; FR-). [63]

The fluorescence image of FA-Au-GQDs treated cells and their mean fluorescence intensity values are shown in Figure 39, respectively. FA-Au-GQDs was successfully internalized into MCF-7 cells and they exhibited more uniform and higher fluorescence than FA-Au-GQDs in SK-BR-3 cells, indicating targeting ability of FA-Au-GQDs for folate receptor positive cells. These data provided upconverted FA-Au-GQDs were capable of visualizing Cys in MCF-7 cells owing to efficient PET process after reaction with Cys. These results are in accordance with the previous reports that mono-boronate group can detect Cys-treated cells.

According to the fluorescence images, FA-Au-GQDs had no considerable change in cell shape. The viabilities of FA-Au-GQDs treated MCF-7 cells were checked *in vitro* (Figure 40). The level of ATP production in FA-Au-GQDs-treated cells exhibited no significant decrease compared to negative control. The lowest viability was about 85% even at a high concentration of FA-Au-GQDs (250 μg mL^{-1}). Previous researches reported that the viability of

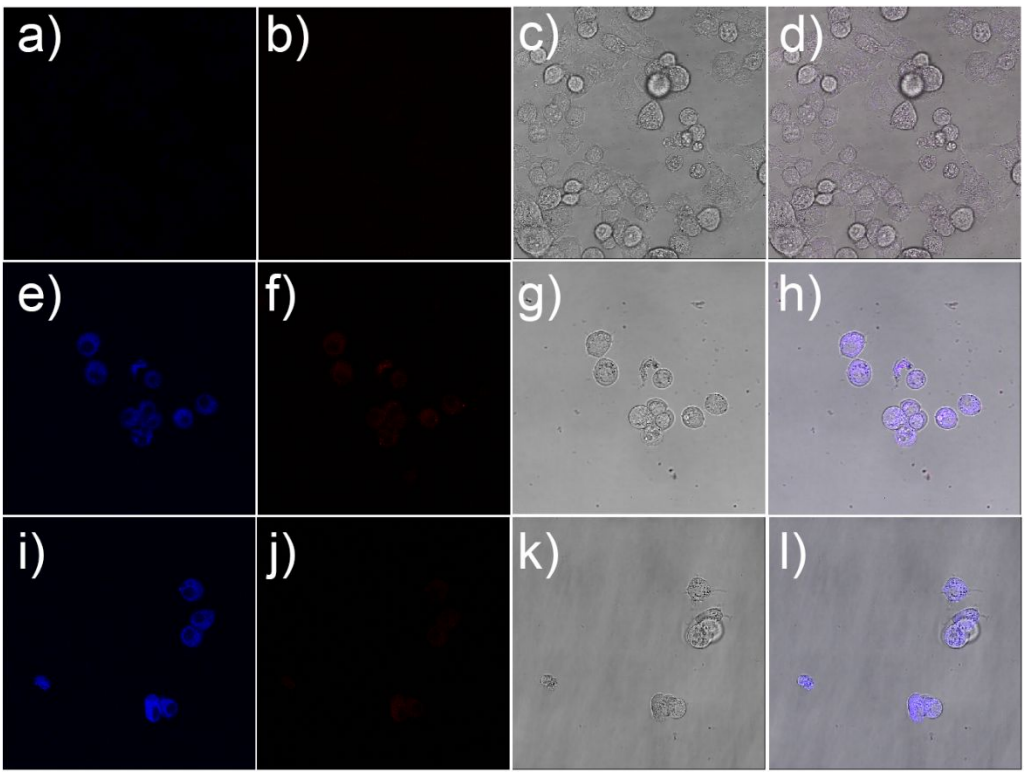

Figure 39. Fluorescence images of SK-BR-3 cells treated with FA-Au-GQDs (0.05 mM).; (a) from blue channel of cells; (b) from red channel; (c) Bright field images (d) fluorescence image. Fluorescence images of MCF-7 cells treated with FA-Au-GQDs (0.05 mM).; (e) from blue channel of cells; (f) from red channel; (g) Bright field images (h) fluorescence image. (i) from blue channel of cells incubated with Cys (0.04 mM) for 30 min; (j) from red channel; (k) Bright field images (l) fluorescence image.

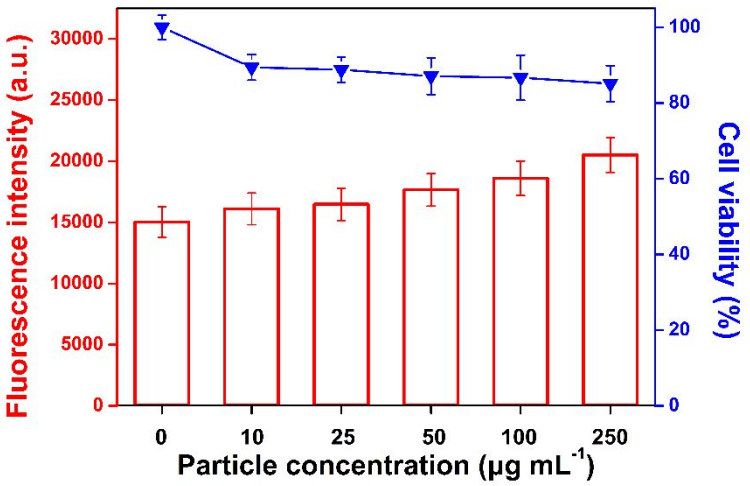

Figure 40. (Red) ROS production by MCF-7 cells after being incubated with FA-Au-GQDs. H_2O_2 (0.02%) was used as a positive control. (Blue) Viability of MCF-7 cells incubated with FA-Au-GQDs for 24 h. The viability was calculated relative to a negative control. Values exhibit mean ± SD, and each experiment was performed in triplicate.

fluorescent polymer nanoparticle-treated cells were about 84% at same concentration. In general, fluorescent GQDs are known as low toxic materials. Based on these data, FA-Au-GQDs can be considered as low toxic materials and are suitable for bio-applications. We further test their ROS generating ability because generating ROS can affect not only toxicity but also accuracy of the fluorescence sensing result of FA-Au-GQDs. As shown in Figure 40, the ROS values showed no significant change compared to negative control, like cell viability results. Therefore, the FA-Au-GQDs is an effective intracellular Cys/Hcy detector without significant ROS production. Judging from these data, FA-Au-GQDs provides ratiometric and selective H_2O_2 detection with low toxicity in only folate positive cells.

4. CONCLUSIONS

1. PAN nanomaterials as novel bioimaging agents without additional fluorophores were developed by ultrasound induced emulsion polymerization. The PAN nanoparticles exhibited the uniform diameter of *ca.* 50 nm and were well dispersible in aqueous media. The PL properties and amidinne/Schiff base dual functional group could be introduced onto the PAN nanoparticles. The fluorescence quantum yield of the tPAN nanoparticles was 11 times higher than that of PAN NPs. In addition, the tPAN nanoparticles exhibited excellent selectivity for copper ions in aqueous solution and mammalian cells, and shows low cytotoxic and well uptaken into the SK-BR-3 cells. These tPAN nanoparticles provided potential platform for detectin copper ions
2. A dual emission Au-PAN NPs sensor was prepared for sensitive detection of mercury ions in aqueous solution. The Au-PAN nanoparticles showed significant intensity change by addtion of mercury ions and higher binding affinity toward mercury ion than other metal ions. Additionally, the 50 nm Au-PAN nanoparticle sensors showed remarkable LOD values, of 1 nM. The fluorescent Au nanocluster decorated PAN nanoparticles provide a new direction for the development of rapid, highly sensitive, and selective sensors and could be subsequently expanded to a platform of versatile

fluorescence detectors.

3. A novel fluorescent Au-GQDs nanoparticle was synthesized for use as a probe that can selectively detect Cys in living cells. A dual emission fluorescence peak ratio changed when the Au-GQDs nanoparticles reacted with Cys. This fluorescence behavior was highly specific for Cys. Additionally, the Au-GQDs nanoparticles these novel nanoparticles to detect changes in Cys concentration was demonstrated in macrophage cells. Considering these observations, the Au-GQDs nanoparticles offer a new way to selectively recognize Cys and cell imaging, and may lead to biomedical applications as an intracellular Cys sensor.

In summary, PAN nanoparticles and GQDs with fluorescence were successfully applied for specific molecule and metal ion detection such as a bioimaging agent, copper and mercury ion detector, and cysteine indicator. First, amidine/Schiff base dual modified PAN NPs were fabricated for intracellular copper ion detection. Second, Au-decorated PAN NPs with dual emission and outstanding selective sensing propertied for mercury ions could attribute a new platform of versatile fluorescence detectors. Third, a novel fluorescent Au-GQDs nanoparticle synthesized for use as a probe were able to be detect Cys in living cells selectively.

These nanoparticles showed enhanced PL intensity *via* PET effect, attachment with various sensing moieties, and biocompatibility. These hybrid nanoprobe offer new platform of potential bio- and chemical-sensor.

REFERENCES

[1] S. Lee, K. Park, K. Kim, K. Choi, I.C. Kwon, *Chem. Commun.,* **2008**, 4250.

[2] M.A. Phillips, M.L. Gran, N.A. Peppas, *Nano Today,* **2010***, 5*, 143.

[3] M. Sumitomo, F. Koizumi, T. Asano, A. Horiguchi, K. Ito, T. Asano, T. Kakizoe, M. Hayakawa, Y. Matsumura, *Cancer Res.,* **2008**, *68*, 1631.

[4] H. Maeda, J. Wu, T. Sawa, Y. Matsumura, K. Hori, *J. Control. Release,* **2000***, 65*, 271.

[5] K. Park, S. Lee, E. Kang, K. Kim, K. Choi, I.C. Kwon, *Adv. Funct. Mater.,* **2009**, *19*, 1553.

[6] X.L. Wu, J.H. Kim, H. Koo, S.M. Bae, H. Shin, M.S. Kim, B.-H. Lee, R.-W. Park, I.-S. Kim, K. Choi, I.C. Kwon, K. Kim, D.S. Lee, *Bioconj. Chem.* **2010**, *21*, 208.

[7] H. Koo, H. Lee, S. Lee, K.H. Min, M.S. Kim, D.S. Lee, Y. Choi, I.C. Kwon, K. Kim, S.Y. Jeong, *Chem. Commun.,* **2010**, *46*, 5668.

[8] K. Kim, J.H. Kim, H. Park, Y.-S. Kim, K. Park, H. Nam, S. Lee, J.H. Park, R.-W. Park, I.-S. Kim, K. Choi, S.Y. Kim, K. Park, I.C. Kwon, *J. Control. Release,* **2010***, 146*, 219.

[9] H. Kobayashi, M. Ogawa, R. Alford, P.L. Choyke, Y. Urano, *Chem. Rev.,* **2009***, 110*, 2620.

[10] S. Lee, J. Xie, X. Chen, *Chem. Rev.*, **2010**, *110*, 3087.

[11] Vasudevanpillai Biju, *Chem. Soc. Rev.,* **2014**, *43*, 744.

[12]L. Sampath, S. Kwon, S. Ke, W. Wang, R. Schiff, M.E. Mawad, E.M. Sevick-Muraca, *J. Nucl. Med.*, **2007**, *48*, 1501.

[13] H. Wang, R. Yang, L. Yang, W. Tan, *ACS Nano,* **2009**, *3*, 2451.

[14] K. Knop, R. Hoogenboom, D. Fischer, U. Schubert, *Angew. Chem. Int. Ed.,* **2010***, 49*, 6288.

[15] C. B. Murray, D. J. Norris and M. G. Bawendi, *J. Am. Chem. Soc.*, **1993**, *115*, 8706.

[16] M. Brust, M. Walker, D. Bethell, D. J. Schiffrin and R. Whyman, *J. Chem. Soc., Chem. Commun.*, **1994**, 801.

[17] M. Giersig and P. Mulvaney, *Langmuir*, **1993**, *9*, 3408.

[18] C. J. Murphy, A. M. Gole, S. E. Hunyadi, J. W. Stone, P. N. Sisco, A. Alkilany, B. E. Kinard and P. Hankins, *Chem. Commun.*, **2008**, 544.

[19] J. Zheng, C. Zhang and R. M. Dickson, *Phys. Rev. Lett.*, **2004**, *93*, 077402.

[20] M. M. Alvarez, J. T. Khoury, T. G. Schaaff, M. N. Shafigullin, I. Vezmar and R. L. Whetten, *J. Phys. Chem. B*, **1997**, *101*, 3706.

[21] E. S. Shibu, S. Sugino, K. Ono, H. Saito, A. Nishioka, S. Yamamura, M. Sawada, Y. Nosaka and V. Biju, *Angew. Chem., Int. Ed.*, **2013**, *52*, 10559.

[22] K. Saha, S. S. Agasti, C. Kim, X. Li and V. M. Rotello, *Chem. Rev.*, **2012**, *112*, 2739.

[23] R. Elghanian, J. J. Storhoff, R. C. Mucic, R. L. Letsinger and C. A. Mirkin, *Science*, **1997**, *277*, 1078.

[24] B. G. Trewyn, I. I. Slowing, S. Giri, H.-T. Chen and V. S.-Y. Lin, *Acc. Chem. Res*., **2007**, *40*, 846.

[25] S.-H. Wu, C.-Y. Mou and H.-P. Lin, *Chem. Soc. Rev.*, **2013**, *42*, 3862.

[26] A. Vinu, K. Z. Hossain and K. Ariga, *J. Nanosci. Nanotechnol.*, **2005**, *5*, 347.

[27] G. T. Hermanson, *Bioconjgate Techniques, Academic Press*, **1996**.

[28] P. Yang, S. Gaib and J. Lin, *Chem. Soc. Rev*., **2012,** *41*, 3679.

[29] M.A. Phillips, M.L. Gran, N.A. Peppas, *Nano Today,* **2010**, *5*, 143.

[30] Z. Guo, S. Park, J. Yoon, I. Shin, *Chem. Soc. Rev.,* **2014**, 43, 16

[31] D.J. Bharali, S.A. Mousa, *Pharmacol. Ther.,* **2010***, 128*, 324.

[32] M.A. Phillips, M.L. Gran, N.A. Peppas, *Nano Today*, **2010**, *5*, 143.

[33] J. Shi, A.R. Votruba, O.C. Farokhzad, R. Langer, *Nano Lett.,* **2010**, 10, 3223.

[34] S.S. Agasti, S. Rana, M.-H. Park, C.K. Kim, C.-C. You, V.M. Rotello, *Adv. Drug Deliv. Rev.,* **2010**, *62*, 316.

[35] N. Karton-Lifshin, E. Segal, L. Omer, M. Portnoy, R. Satchi- Fainaro and D. Shabat, *J. Am. Chem. Soc.*, **2011**, *133*, 10960.

[36] Z. Guo, S. W. Nam, S. Park and J. Yoon, *Chem. Sci.*, **2012**, *3*, 2760.

[37] P. Li, X. Duan, Z. Chen, Y. Lin, T. Xie, L. Fang, X. Li, M. Yin and B. Tang, *Chem. Commun.*, **2011**, *47*, 7755.

[38] Z. Guo, W. Zhu, M. Zhu, X. Wu and H. Tian, *Chem. Eur. J.*, **2010**, *16*, 14424.

[39] Z. Luo, X. Yuan, Y. Yu, Q. Zhang, D.T. Leong, J.Y. Lee, J. Xie, *J. Am. Chem. Soc.*, **2012**, *134*, 16662

[40] D. Wu, Z. Chen, G. Huang, X. Liu, *Sens. Actuators A*, **2014**, *205*, 72.

[41] J. Zhao, J. Deng, Y. Yi, H. Li, Y. Zhang, S. Yao, *Talanta*, **2014**, *125*, 372.

[42] A. M. Derfus, W. C. W. Chan, S. N. Bhatia, *Nano Lett.,* **2003**, *4*, 11.

[43] A. Zhu, Q. Qu, X. Shao, B. Kong, Y. Tian, *Angew. Chem., Int. Ed.,* **2012**, *51*, 7185

[44] K. J. Lee, W.-K. Oh, J. Song, S. Kim, J. Lee, J. Jang, *Chem. Commun*., **2010**, *46*, 5229.

[45] W. K. Oh, Y. S. Jeong, J. Song, J. Jang, *Biosens. Bioelectron.,* **2011**, *29*, 172.

[46] K. J. Lee, J. H. Oh, Y. Kim, J. Jang, *Adv. Mater.,* **2006**, *18*, 2216.

[47] L. Yang, W. Zhu, M. Fang, Q. Zhang, C. Li, *Spectrochim. Acta, Part A,* **2013**, *109*, 186.

[48] S.-H. Huang, G. J. Jiang, D.-J. Liaw, C.-L. Li, C.-C. Hu, Lee, K.-R. Lai, J.-Y. *J. Appl. Polym. Sci.,* **2009**, *114*, 1511.

[49] M. H. Lee, T. V. Giap, S. H. Kim, Y. H. Lee, C. Kang, J. S. Kim, *Chem. Commun.,* **2010**, *46*, 1407.

[50] P. Kampalanonwat, P. Supaphol, *ACS Appl. Mater. Interfaces,* **2010**, *2*, 3619.

[51] Z. Li, L. Zhang, L. Wang, Y. Guo, L. Cai, M. Yu, L. Wei, *Chem. Commun*., **2011**, *47*, 5798.

[52] Y. Hong, S. Chen, C. W. T. Leung, J. W. Y. Lam, J. Liu, N.-W. Tseng, R. T. K. Kwok, Y. Yu, Z. Wang, B. Z. Tang, *ACS Appl. Mater. Interfaces,* **2011**, *3*, 3411.

[53] M. A. H. Muhammed, P. K. Verma, S. K. Pal, A. Retnakumari, M. Koyakutty, S. Nair, T. Pradeep, *Chem-Eur. J.*, **2010**, *16*, 10103.

[54] L. Yang, W. Zhu, M. Fang, Q. Zhang, C. Li, *Acta Pt. A-Molec. Biomolec. Spectr.,* **2013**, *109*, 186.

[55] S. Chowdhury, Z. Wu, A. J. Gerstl, S. Liu, A. Dembska, B. A. Armitage, R. Jin, L. A. Peteanu, *J. Phys. Chem. C,* **2011**, *115*, 20105.

[56] C. S. Yun, A. Javier, T. Jennings, M. Fisher, S. Hira, S. Peterson, B. Hopkins, N. O. Reich, G. F. Strouse, *J. Am. Chem. Soc.*, **2005**, *127*, 3115.

[57] D. Li, A. Wieckowska, I. Willner, *Angew. Chem.*, **2008**, *120*, 3991.

[58] Z. D. Wang, J. H. Lee, Y. Lu, *Chem. Commun.*, **2008**, 6005

[59] E. Lee, J. Ryu, J. Jang, *Chem. Commun.* **2013**, *49*, 9995.

[60] T. Shu, L. Su, J. Wang, C. Li, X. Zhang, *Biosens. Bioelectron.*, **2015**, *66*, 155.

[61] C. Kim, S. Kim, W. K. Oh, M. Choi, J. Jang, *Chem. Eur. J.* **2012**, *18*, 4902.

[62] W.-K. Oh, Y. S. Jeong, S. Kim, J. Jang, *ACS Nano,* **2012**, *6*, 8516.

[63] Y. Tao, Y. Lin, Z. Huang, J. Ren, X. Qu, *Adv. Mater.* **2013**, *25*, 2594.

국문초록

최근 나노 크기의 단일시스템 안에서 다양한 요소들을 도입하는 연구가 생명과학 분야에서 많은 관심을 받고 있다. 기존의 물질이나 단일 요소로 구성된 나노 물질에 비해서 복합 나노 물질은 다양한 분야에서 매우 뛰어난 성능을 발휘하며 향상된 기능성을 가지고 있다는 장점이 있다. 이에 나노 기술의 발전과 함께 복합 나노 물질을 제조하는 연구가 활발히 진행되고 있다. 나노 입자는 이런 복합성을 가질 수 있는 가장 기본적인 구조이며, 구성에 따라서 복합 나노 입자는 다른 나노 구조체에 비해 세포 내에 가장 많이 도입될 수 있는 장점을 가질 수 있다. 하지만, 생명과학 분야에 적합한 복합 나노 입자를 제조하는 연구에 관한 보고는 여전히 부족한 실정이다.

본 연구에서는 형광 복합 나노 입자를 제조하여 특정 이온 및 분자의 검출을 평가하고 본 입자를 수용액 또는 세포 내에서의 특정 물질 검출에 응용하였다. 본 연구는 아미딘을 도입한 폴리아크릴로니트릴의 세포 내 구리 이온 검출 응용, 금 나노 입자를 도입한 폴리아크릴로니트릴 기반 복합 나노 입자를 이용한 수은 이온 검출 응용, 그리고 금 나노 입자를 도입한 그래핀 양자점 기반 복합 나노 입자를 이용한 세포 내 시스테인 검출 응용, 이렇게 총 세 개의 부분으로 구성되어 있다.

아미딘이 도입된 폴리아크릴로니트릴 나노 입자는 초음파 매개 에멀젼 중합을 통해 제조되었으며, 피너 방법을 통해 아미딘 그룹으로

표면이 개질되었다. 생체친화성을 가지고 있는 형광 아미딘-폴리아크릴로니트릴 나노입자는 살아있는 세포 안에 있는 구리 이온에 대해 높은 민감도와 선택성을 가지는 센서 개발에 있어 새로운 방향성을 제시하여 주었다.

금 나노 입자를 합성하여 이를 폴리아크릴로니트릴 나노 입자 표면에 도입하였으며, 이에 두 가지 형광을 동시에 발휘하는 복합 나노 입자를 제조하였다. 금 나노 입자가 도입된 폴리아크릴로니트릴 복합 나노 입자에 호모시스테인과 머캡토프로피온산을 반응시켜 수은 이온을 선택적으로 검출할 수 있는 작용기를 도입하였다. 이중 형광 특성은 수은 이온에 대해 높은 선택성을 발휘하였으며, 또한 농도에 따른 직선 비례적인 검출 수준과 높은 민감도의 검출 한계 역시 나타내었다.

금 나노 입자를 합성하여 이를 그래핀 양자점 표면에 도입하였으며 이에 두가지 형광을 동시에 발휘하는 복합 나노 입자를 제조하였다. 제조된 복합 나노 입자의 금 나노 입자는 시스테인과 싸이올 본드를 형성하여 수 많은 아미노산 중 머캡토 아미노산에 대해 선택적 검출 능력을 보여주었다. 또한 농도에 따른 직선 비례적인 검출 수준과 높은 민감도의 검출 한계를 보여줌으로써 이중 형광 복합 나노 입자의 효과적인 시스테인 검출 특성을 증명하였다. 낮은 독성을 가지고 있는 금 나노 입자-그래핀 양자점 복합 나노 입자는 생체 내에서 효과적으로 세포를 이미징하는 에이전트로 적용이 될 수 있으며 동시에 특정 아미노산을

감지하는 센서로도 적용될 수 있다.

본 연구에서 형광 복합 나노 입자를 제조하는 다양한 방법과 생명과학분야 응용 가능성에 대해 평가하였다. 본 연구에서 제조된 형광 복합 나노 입자들은 특정 금속 이온과 특정 아미노산 센서 그리고 세포 이미징 에이전트 분야에 응용하였다. 본 입자들은 각각의 응용에 적합하고 최적의 성능을 낼 수 있도록 디자인되고 제조되었다. 이러한 결과들은 다양한 형광 복합 나노 입자를 제조하고 이를 생명과학분야에 적용하는 것에 관한 양질의 정보들을 제공하게 될 것이다.

주요어: 형광 복합 나노입자, 표면 개질, 금 나노 입자, 그래핀 양자점, 세포 이미징, 형광 검출

학번: 2013-31307